Supporting Information

MOF-derived M-OOH with rich oxygen defects by in-situ electro-oxidation reconstitution for highly efficient oxygen evolution reaction

Zhikai Shi[a], Zebin Yu[a], Ronghua Jiang[b], Jun Huang[c], Yanping Hou[a], Jianhua Chen[a], Yongqing Zhang[d], Hongxiang Zhu[e], Bing Wang[f], Han Pang[a]*

[a] MOE Key Laboratory of New Processing Technology for Non-ferrous Metals and Materials, Guangxi Key Laboratory of Processing for Non-ferrous Metals and Featured Materials, School of Resources, Environment & Materials, Guangxi University, Nanning 530004, P. R. China.

[b] School of Chemical & Environmental Engineering, Shaoguan University, Shaoguan 512005, P. R. China

[c] College of Civil Engineering & Architecture, Guangxi University, Nanning 530004, P. R. China

[d] School of Environment & Energy, Guangdong Provincial Key Laboratory of Atmospheric Environment and Pollution Control, South China University of Technology, Guangzhou 510640, P. R. China.

[e] Guangxi Key Laboratory of Clean Pulp & Papermaking and Pollution Control, Nanning, 530004, P.R. China

[f] College of Resource & Environment Engineering, Guizhou University, Guiyang, 550025, P. R. Chin

Corresponding Author: School of Resources, Environment & Materials, Guangxi University,

Nanning 530004, P. R. China; Tel./fax.: + 8613877108420; E-mail: xxzx7514@hotmail.com

Content

Physical characterization

Electrochemical measurements

In-situ Raman experiments

Density functional theory (DFT) calculations

Fig. S1. (a) TEM image of Fe_2Co-MOF. (b) Strain map of Fe_2Co-MOF.

Fig. S2. (a) TEM image of Fe_2Co-MOF@M-OOHv-ER. (b) Strain map of Fe_2Co-MOF@M-OOHv-ER.

Fig. S3. (a) Ar_2 adsorption/desorption isotherms of NF, Fe_2Co-MOF/NF, and Fe_2Co-MOF@M-OOHv-ER/NF, respectively. (b) The pore size distribution of NF, Fe_2Co-MOF/NF, and Fe_2Co-MOF@M-OOHv-ER/NF, respectively. (c) A comparison with the relevant materials.

Fig. S4. SEM images of (a, b, c, d) Co-MOF/NF, (e, f, g, h) FeCo-MOF/NF, (i, j, k, l) Fe_3Co-MOF/NF, and (a, b, c, d) Fe-MOF/NF at 100um, 2um, 1um, and 500nm, respectively.

Fig. S5. SEM images of (a, b, c, d) Fe_3Co-MOF/NF-3 h, and (e, f, g, h) Fe_3Co-MOF/NF-9 h at 100um, 2um, 1um, and 500nm, respectively.

Fig. S6. SEM images of (a, b, c, d) Fe_3Co-MOF/NF-140 °C, and (e, f, g, h) Fe_3Co-MOF/NF-180 °C at 100um, 2um, 1um, and 500nm, respectively.

Fig. S7. SEM images of (a, b, c, d) Fe_2Co-MOF@M-OOHv-ER/NF-2nd, and (e, f, g, h) Fe_2Co-MOF@M-OOHv-ER/NF-30thth at 100um, 2um, 1um, and 500nm, respectively.

Fig. S8. SEM images of (a, b, c, d) Fe_2Co-MOF@M-OOHv-ER/NF-0.1 M KOH, and (e, f, g, h) Fe_2Co-MOF@M-OOHv-ER/NF-5 M KOH at 100um, 2um, 1um, and 500nm, respectively.

Fig. S9. SEM-EDX elemental mapping of (a, b, c, d, e, f) Fe_2Co-MOF/NF, and (g, h, i, j, k, l)

Fe₂Co-MOF@M-OOHv-ER/NF.

Fig. S10. (a)XRD patterns of Fe/Co-MOF/NF samples with different mole ratios (Fe:Co = 1:0, 1:1, 2:1, 3:1, 0:1). (b) FT-IR spectrums of Fe/Co-MOF/NF samples with different mole ratios (Fe: Co = 1:0, 1:1, 2:1, 3:1, 0:1). (c)XRD patterns of Fe/Co-MOF/NF samples with different synthesis temperature (140 ℃, 160 ℃, 180 ℃). (d) FT-IR spectrums of Fe/Co-MOF/NF samples with different synthesis temperature (140 ℃, 160 ℃, 180 ℃). (e)XRD patterns of Fe/Co-MOF/NF samples with different synthesis time (3 h, 6 h, 9 h). (f) FT-IR spectrums of Fe/Co-MOF/NF samples with different synthesis time (3 h, 6 h, 9 h).

Fig. S11. (a)XRD patterns of Fe₂Co-MOF@M-OOHv-ER/NF samples with different cycles (2nd, 20th, 30thth). (b) FT-IR spectrums of Fe₂Co-MOF@M-OOHv-ER/NF samples with different cycles (2nd, 20th, 30thth). (c)XRD patterns of Fe₂Co-MOF@M-OOHv-ER/NF samples with different KOH concentrations (0.1 M KOH, 1 M KOH, 5 M KOH). (d) FT-IR spectrums of Fe₂Co-MOF@M-OOHv-ER/NF samples with different KOH concentrations (0.1 M KOH, 1 M KOH, 5 M KOH).

Fig. S12. Fluorescence spectra of Fe₂Co-MOF/NF, and Fe₂Co-MOF@M-OOHv-ER/NF at excitation wavelengths of 285 nm.

Fig. S13. (a) IR-compensation LSV curves of Fe/Co-MOF/NF samples with different mole ratios (Fe:Co = 1:0, 1:1, 2:1, 3:1, 0:1) for OER in 1 M KOH. (b) Tafel slopes of the above electrodes. (c) Nyquist plots recorded at open circuit voltage in the frequency range from 100 kHz–0.01 Hz. (d) Plots used for evaluating the ECSA as a function of scan rate.

Fig. S14. (a) IR-compensation LSV curves of Fe/Co-MOF/NF samples with different synthesis time (3 h, 6 h, 9 h) for OER in 1 M KOH. (b) Tafel slopes of the above electrodes. (c) Nyquist

plots recorded at open circuit voltage in the frequency range from 100 kHz–0.01 Hz. (d) Plots used for evaluating the ECSA as a function of scan rate.

Fig. S15. (a) IR-compensation LSV curves of Fe/Co-MOF/NF samples with different synthesis temperature (140 °C, 160 °C, 180 °C) for OER in 1 M KOH. (b) Tafel slopes of the above electrodes. (c) Nyquist plots recorded at open circuit voltage in the frequency range from 100 kHz–0.01 Hz. (d) Plots used for evaluating the ECSA as a function of scan rate.

Fig. S16. (a) IR-compensation LSV curves of Fe_2Co-MOF@M-OOHv-ER/NF samples with different cycles (2nd, 20th, 30thth) for OER in 1 M KOH. (b) Tafel slopes of the above electrodes. (c) Nyquist plots recorded at open circuit voltage in the frequency range from 100 kHz–0.01 Hz. (d) Plots used for evaluating the ECSA as a function of scan rate.

Fig. S17. (a) IR-compensation LSV curves of Fe_2Co-MOF@M-OOHv-ER/NF samples with different KOH concentrations (0.1 M KOH, 1 M KOH, 5 M KOH) for OER in 1 M KOH. (b) Tafel slopes of the above electrodes. (c) Nyquist plots recorded at open circuit voltage in the frequency range from 100 kHz–0.01 Hz. (d) Plots used for evaluating the ECSA as a function of scan rate.

Fig. S18. (a) CV curves of Co-MOF/NF; (b) CV curves of FeCo-MOF/NF;(c) CV curves of Fe_3Co-MOF/NF; (d) CV curves of Fe-MOF/NF; (e) CV curves of Fe_2Co-MOF/NF-3 h; (f) CV curves of Fe_2Co-MOF/NF-9 h; (g) CV curves of Fe_2Co-MOF/NF-140 °C;(h) CV curves of Fe_2Co-MOF/NF-180 °C; (i) CV curves of Fe_2Co-MOF@M-OOHv-ER/NF-2nd; (j) CV curves of Fe_2Co-MOF@M-OOHv-ER /NF-30thth; (k) CV curves of Fe_2Co-MOF@M-OOHv-ER/NF-0.1 M KOH; (l) CV curves of Fe_2Co-MOF@M-OOHv-ER/NF-5 M KOH; (m) CV curves of NF; (n) CV curves of Fe_2Co-MOF/NF; (o) CV curves of Fe_2Co-MOF@M-OOHv-ER/NF; (P)

CV curves of Fe$_2$Co-MOF@M-OOHv/NF at increasing scan rates from 10 mV s^{-1} to 50 mV s^{-1}.

Fig. S19. (a) XRD patterns of Fe$_2$Co-MOF@M-OOHv-ER/NF before and after the stability test; (b) FTIR patterns of Fe$_2$Co-MOF@M-OOHv-ER/NF before and after the stability test; (c) XPS patterns for the O 1s of Fe$_2$Co-MOF@M-OOHv-ER/NF before and after the stability test; (d) PL patterns of Fe$_2$Co-MOF@M-OOHv-ER/NF before and after the stability test. TEM images of (e, f) Fe$_2$Co-MOF@M-OOHv-ER/NF after the stability test.

Fig. S20. (a) Photographs of oxygen collected at various reaction times. (b) Faraday efficiency and the volum of O$_2$ of the Fe$_2$Co-MOF@M-OOHv-ER/NF for OER at various reaction time. (c) The photograph of Faraday efficiency test.

Fig. S21. SEM images of (a, b, c, d) Fe$_2$Co-MOF@M-OOHv-ER/NF at 100um, 2um, 1um, and 500nm, respectively. SEM-EDX elemental mapping of (e, f, g, h, i, j) Fe$_2$Co-MOF@M-OOHv-ER/NF. TEM and HR-TEM images of (k, l) Fe$_2$Co-MOF@M-OOHv-ER/NF. (m) Strain map of Fe$_2$Co-MOF@M-OOHv-ER/NF. (n)XRD pattern of Fe$_2$Co-MOF@M-OOHv-ER/NF. (o) FT-IR spectrum of Fe$_2$Co-MOF@M-OOHv-ER/NF.

Fig. S22. (a) XPS full survey of Fe$_2$Co-MOF@M-OOH/NF. HR-XPS spectra of (b) C1s, (c) O1s, (d) Ni2p, (e) Fe2p, and (f) Co2p of Fe$_2$Co-MOF@M-OOH/NF.

Fig. S23. (a) IR-compensation LSV curves of Fe$_2$Co-MOF/NF, Fe$_2$Co-MOF@M-OOH/NF and Fe$_2$Co-MOF@M-OOHv-ER/NF for OER in 1 M KOH. (b) Tafel slopes of the above electrodes. (c) Nyquist plots recorded at open circuit voltage in the frequency range from 100 kHz–0.01 Hz. (d) Plots used for evaluating the ECSA as a function of scan rate.

Fig. S24. (a) IR-compensation LSV curves of Fe/Co-MOF/NF samples with different mole ratios (Fe:Co = 1:0, 1:1, 2:1, 3:1, 0:1) for OER in 1 M KOH. (b) Tafel slopes of the above

electrodes. (c) IR-compensation LSV curves of Fe/Co-MOF/NF samples with different synthesis time (3 h, 6 h, 9 h) for OER in 1 M KOH. (d) Tafel slopes of the above electrodes. (e) IR-compensation LSV curves of Fe/Co-MOF/NF samples with different synthesis temperature (140 °C, 160 °C, 180 °C) for OER in 1 M KOH. (f) Tafel slopes of the above electrodes.

Fig. S25. (a) Stability test for HER at 100 mA cm^{-2} by Fe$_2$Co-MOF/NF electrode in 1 M KOH solution. (b) XRD patterns of Fe$_2$Co-MOF/NF before and after the stability test; (c) FTIR patterns of Fe$_2$Co-MOF/NF before and after the stability test. TEM images of (e, f) Fe$_2$Co-MOF/NF after the stability test.

Fig. S26. Schematic drawings of the crystal structures of (a) FeOOH, (b) FeOOHv, (c) CoOOH, (d) CoOOHv, (e) FeCoOOH, and (f) FeCoOOHv. The Fe, Co, O and H atoms are represented by gray, cyan, red and white spheres, respectively.

Fig. S27. Schematic drawings of the crystal structures of unit cell of (a) FeOOH, (b) FeOOHv, (c) CoOOH and (d) CoOOHv. (e) The projected density of states and band structure of FeOOH and FeOOHv structures. (f) The projected density of states and band structure of CoOOH and CoOOHv structures. The Fe, Co, O and H atoms are represented by gray, cyan, red and white spheres, respectively.

Fig. S28. The adsorption energy of water molecules on the surface of FeCoOOH (a, b), FeCoOOHv-1 (c, d), and FeCoOOHv-2 (e, f). The Fe, Co, O and H atoms are represented by gray, cyan, red and white spheres, respectively.

Fig. S29. The adsorption energy of water molecules on the surface of FeOOH (a, b), FeOOHv (c, d), CoOOH (e, f) and CoOOHv (g, h). The Fe, Co, O and H atoms are represented by gray, cyan, red and white spheres, respectively.

Fig. S30. Photographs of the contact angle of Fe_2Co-MOF@M-OOHv-ER/NF with the H_2O.

Table. S1 The ratios of Fe^{3+}/Fe^{2+} and Co^{3+}/Co^{2+} of the Fe_2Co-MOF/NF and Fe_2Co-MOF@M-OOHv-ER/NF integrated from the XPS, respectively.

Table. S2 The OER overpotentials and Tafel values of the electrodes.

Table. S3 The ECSAs values and EIS values of the electrodes.

Table. S4 The HER overpotentials and Tafel values of the electrodes.

Table. S5 The total energy and the adsorption energy of water molecules of FeCoOOH, FeCoOOHv-1, FeCoOOHv-2.

Table. S6 The total energy and the adsorption energy of water molecules of FeOOH, CoOOH, FeOOHv, CoOOHv.

Table. S7 Comparison of electrochemical performances of OER of Fe_2Co-MOF@M-OOHv-ER/NF with recently reported top tier metal based inorganic OER electrocatalysts in 1 M KOH.

Physical characterization

The crystalline phases of various electrodes were analyzed by Xray diffraction (XRD) using a diffractometer (XRD, DX-2700A, China) with Cu Ka radiation and an accelerating voltage of 40 kV in the 2θ range of 5–90°, at a scanning rate of 15° min^{-1}. The electrode surface morphologies were characterized by a field-emission scanning electron microscopy (FESEM, Hitachi SU8020, Japan), and the elemental compositions of the electrodes were investigated by an energy-dispersive X-ray spectroscopy (EDS). Transmission electron microscopy (TEM) was carried out to characterize the inner structures of the catalysts using a FEI TECNAI G2 F30 instrument from USA at 300 kV. Fourier transform infrared spectroscopy (FT-IR) was recorded on a Nicolet iS 50 FTIR spectrometer from USA with scans from 4000 to 400 cm^{-1}. X-ray photoelectron spectroscopy (XPS) was performed to gain insight into the chemical composition and binding states of the electrodes on an ESCALAB 250XI (USA) instrument with a monochromatic Al Ka X-ray source. Using the OmniFluo-960 fluorescence spectrum test system, photoluminescence (PL) spectra was obtained at excitation wavelengths of 285 nm. The contact angle between the liquid and the electrode was measured using the KRUSS DSA100 optical contact angle measuring instrument (Germany). Argon adsorption-desorption isotherms was applied to examine the specific surface areas and the pore size distribution via the Brunauer–Emmett–Teller (BET; TriStar II 3flex, America) and Barrett–Joyner–Halenda (BJH) methods at 87 K.

Electrochemical measurements

All electrochemical measurements were conducted using an electrochemical workstation (CHI 660E, China) using a typical three-electrode system in a quartz electrolytic cell, with the
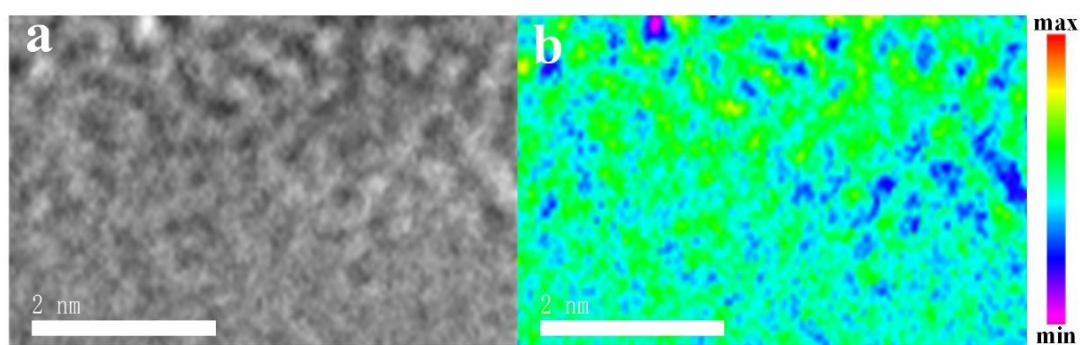
prepared catalyst materials as the working electrode, a Graphite rod electrode as the counter electrode, a Hg|HgO|OH⁻ electrode as the reference electrode, and 1 M KOH as the electrolyte. Since the oxygen evolution reaction is the formation of oxygen after the hydroxide ion loses electrons, the test of the oxygen evolution reaction is usually carried out in an alkaline environment. Before the electrochemical tests, the electrolyte was purged with N_2 for 30 min to remove O_2. The potential values in this study were converted and referred to the reversible hydrogen electrode (RHE) using the Nernst equation, E(RHE)= E (vs. Hg|HgO|OH⁻) + 0.059*pH + 0.098 V= E (vs. Hg|HgO|OH⁻) + 0.924 V. The overpotential (η) was calculated by using the equation: η = E(RHE) − 1.23 V for the OER at 25 °C. Linear sweep voltammetry (LSV) polarization curves for the OER and HER were conducted at a scan rate of 5 mV s⁻¹ with 95% iR compensation. The durability was tested at current densities of 100 mA cm⁻² for 100 h for the HER and OER. Electrochemical impedance spectroscopy (EIS) was performed within the frequency range of 100 kHz to 0.01 Hz with an AC potential amplitude of 5 mV at open circuit voltage for the HER and OER. The electrochemically active surface areas (ECSAs) of the electrodes were characterized by conducting cyclic voltammetry (CV) with various scan rates of 10, 20, 30, 40 and 50 mV s⁻¹ in the non-faradaic region within the potential range from 0.124 V to 0.324 V (vs. RHE). The ECSAs value is equal to the ratio of the dual-layer capacitances (C_{dl}) of the substance to the normally accepted reference specific capacitance (C_s= 0.040 mF cm⁻²). The timed drainage method was used to measure the Faraday efficiency (η = $4N/Q$, N is the number of molecules of oxygen produced, Q the number of electrons consumed) for OER in 1 M KOH.
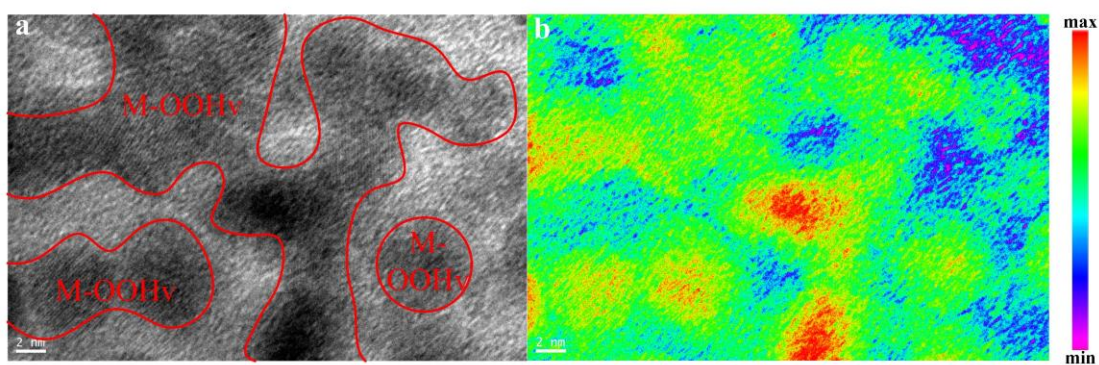
In-situ Raman experiments

A specially made Teflon based electrochemical cell was used for the combined electrochemical and in situ Raman spectroscopy study. This cell contains a Pt wire and an Hg/HgO⁻ electrode, served as the counter and reference electrodes, respectively. The Fe_2Co-MOF/NF electrode was used as the working electrode. In situ Raman spectra of the sample electrodes were recorded using a confocal Raman microscope (Hitachi High-tech SU8020). The laser beam (532 nm, green) was focused through a microscope objective (×50) onto a circular area of 2mm in diameter on the Fe_2Co-MOF/NF electrode and the backscattered light was collected through the same objective. The in-situ Raman experiments were conducted at increasing CV cycles from 0 to 20 cycles (from 0 to 1.2 V vs Hg/HgO⁻ in 1 M KOH at the scan rate of 50 mV s⁻¹) by using green (532 nm) excitation laser lines.

Density functional theory (DFT) calculations

The density of states of M-OOH and M-OOHv were studied using the electronic structure obtained from the periodic density functional theory (DFT) calculations performed through the CASTEP code. Generalized gradient approximation (GGA) for the exchange-correlation using Perdew, Burke and Emzerhof (PBE) was employed to examine the electronic structure for both M-OOH and M-OOHv. For this simulation, the Quality, the Energy cutoff and the k-point were set as fine, 571.40eV and 5x6x8, respectively. The adsorption energy of water molecules was also calculated, and the calculation formula is $\Delta E_{ad}(x) = E_{H_2O\ on\ x} - E_x - E_{H_2O}$, in which x refers to different materials.
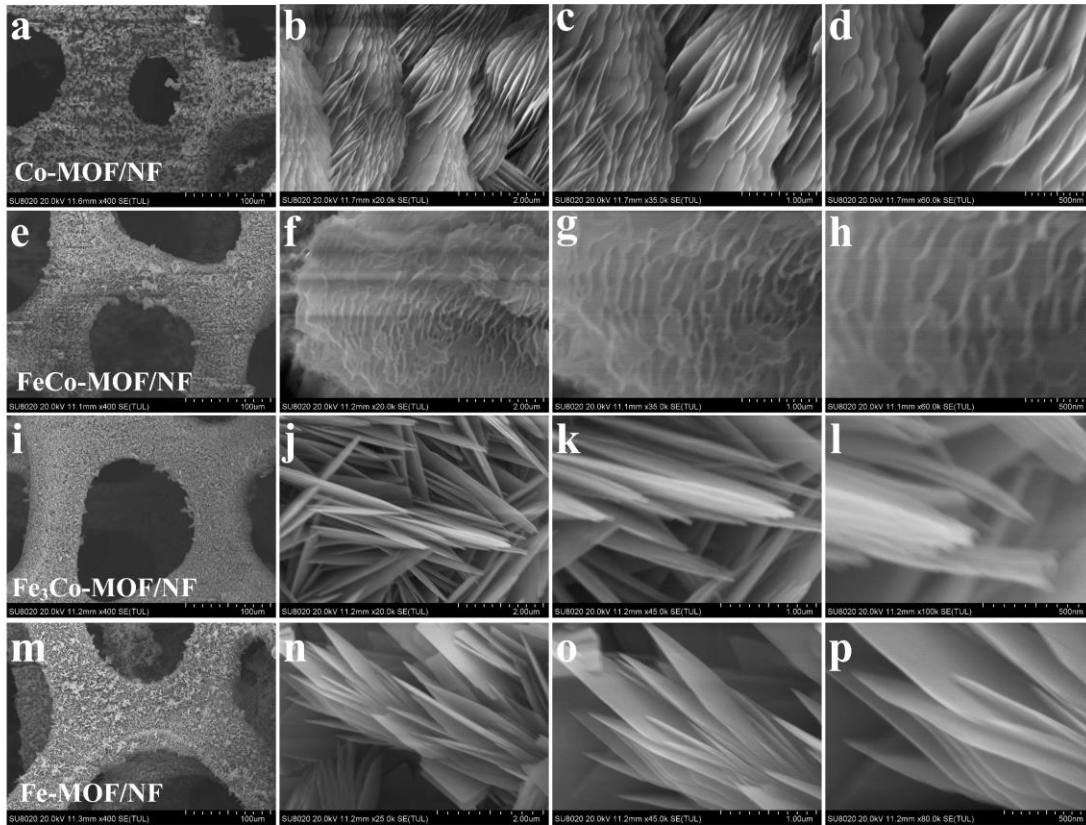
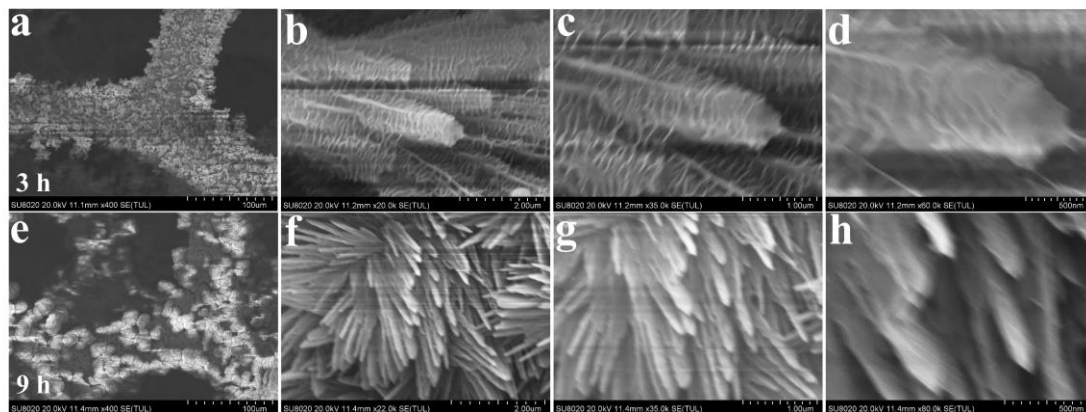**Fig. S1.** (a) TEM image of Fe_2Co-MOF. (b) Strain map of Fe_2Co-MOF.

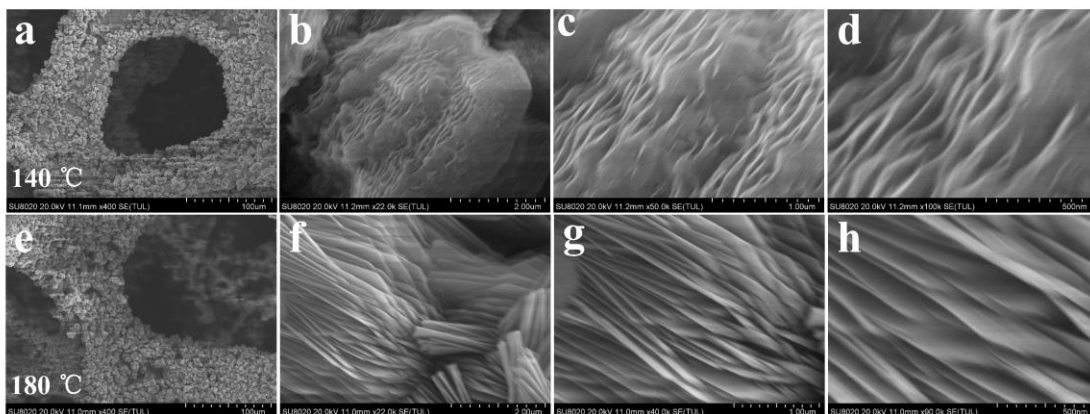**Fig. S2.** (a) TEM image of Fe_2Co-MOF@M-OOHv-ER. (b) Strain map of Fe_2Co-MOF@M-OOHv-ER.

Fig. S3. (a) Ar$_2$ adsorption/desorption isotherms of NF, Fe$_2$Co-MOF/NF, and Fe$_2$Co-MOF@M-OOHv-ER/NF, respectively. (b) The pore size distribution of NF, Fe$_2$Co-MOF/NF, and Fe$_2$Co-MOF@M-OOHv-ER/NF, respectively. (c) A comparison with the relevant materials.

Fig. S4. SEM images of (a, b, c, d) Co-MOF/NF, (e, f, g, h) FeCo-MOF/NF, (i, j, k, l) Fe$_3$Co-MOF/NF, and (a, b, c, d) Fe-MOF/NF at 100um, 2um, 1um, and 500nm, respectively.

Fig. S5. SEM images of (a, b, c, d) Fe$_3$Co-MOF/NF-3 h, and (e, f, g, h) Fe$_3$Co-MOF/NF-9 h at 100um, 2um, 1um, and 500nm, respectively.

Fig. S6. SEM images of (a, b, c, d) Fe₃Co-MOF/NF-140 ℃, and (e, f, g, h) Fe₃Co-MOF/NF-180 ℃ at 100um, 2um, 1um, and 500nm, respectively.

Fig. S4 shows the scanning electron microscope (SEM) images of Co-MOF/NF, FeCo-MOF/NF, Fe₃Co-MOF/NF, and Fe-MOF/NF at 100um, 2um, 1um, and 500nm, respectively. The SEM images of low resolutions reveal that all four MOFs were grown uniformly with full coverage on the skeleton surfaces of NF, respectively (Fig. S4a, 1e, 1i, and 1 M). And as evident from the corresponding high-resolution SEM images, single metal organic frame has a distinctive appearance, such as Co-MOF/NF with stacked leafy large flakes (Fig. S4b-d), and Fe-MOF/NF with needle-like larger flakes (Fig. S4n-p). Correspondingly, the bimetallic organic frameworks present a process of evolution from leaf-like flakes to needle-like flakes, as the proportion of Fe:Co increases (Fig. S4f-h, Fig.1b, and Fig. S4j-l). In addition, the SEM images of electrode materials with different synthesis time (3 h, 9 h) and different synthesis temperature (140 ℃, 180 ℃) were also exhibited (Fig. S5 and S5). With the increase of the synthesis time, flakes begin to appear at 3 h, the specific surface area of the electrode begins to increase. At 9 h, the appearance of the electrode has become completely rod-shaped, and the specific surface area of the electrode is reduced. Moreover, as the synthesis temperature increases, the stacking

degree of the material flakes is different. When the synthesis temperature is 140 ℃, the material has a sparse flake morphology. When the synthesis temperature is 180 ℃, the flakes become thicker and accumulate seriously. Obviously, Fe_2Co-MOF at 6 h and 140 ℃ has the largest specific surface area, which might have the best electrocatalytic performance.
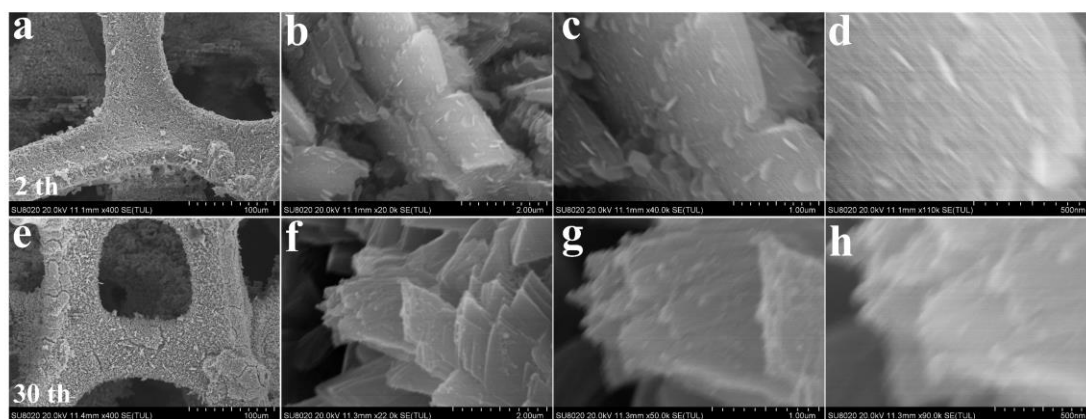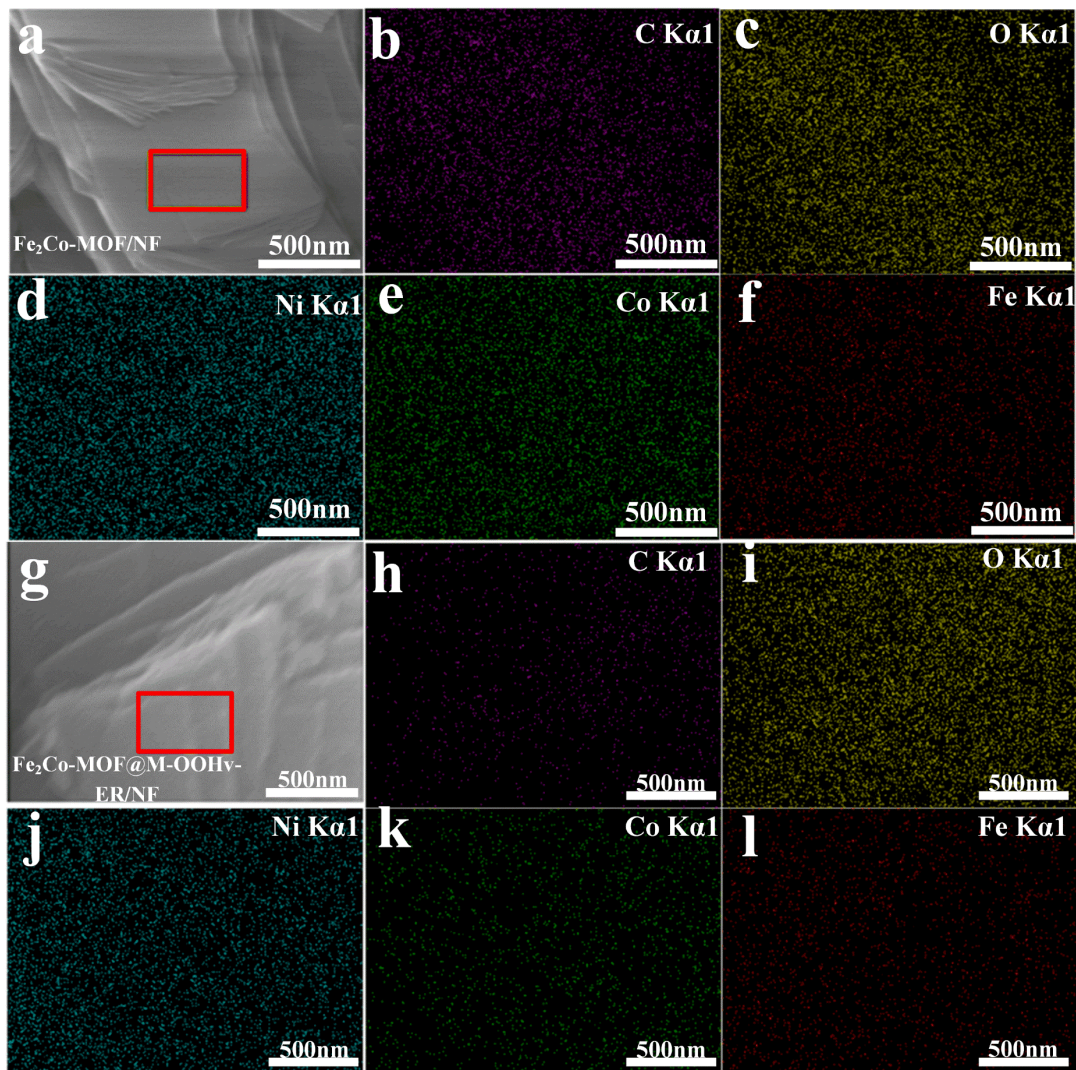

Fig. S7. SEM images of (a, b, c, d) Fe_2Co-MOF@M-OOHv-ER/NF-2nd, and (e, f, g, h) Fe_2Co-MOF@M-OOHv-ER/NF-30thth at 100um, 2um, 1um, and 500nm, respectively.
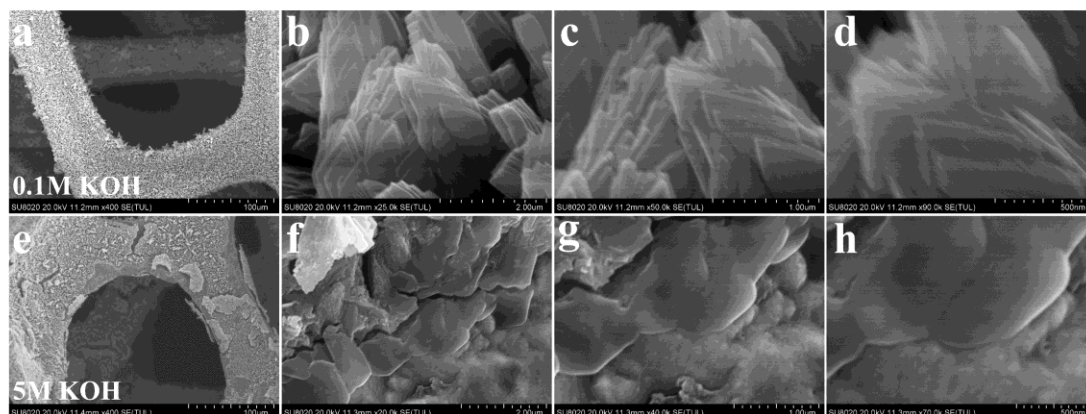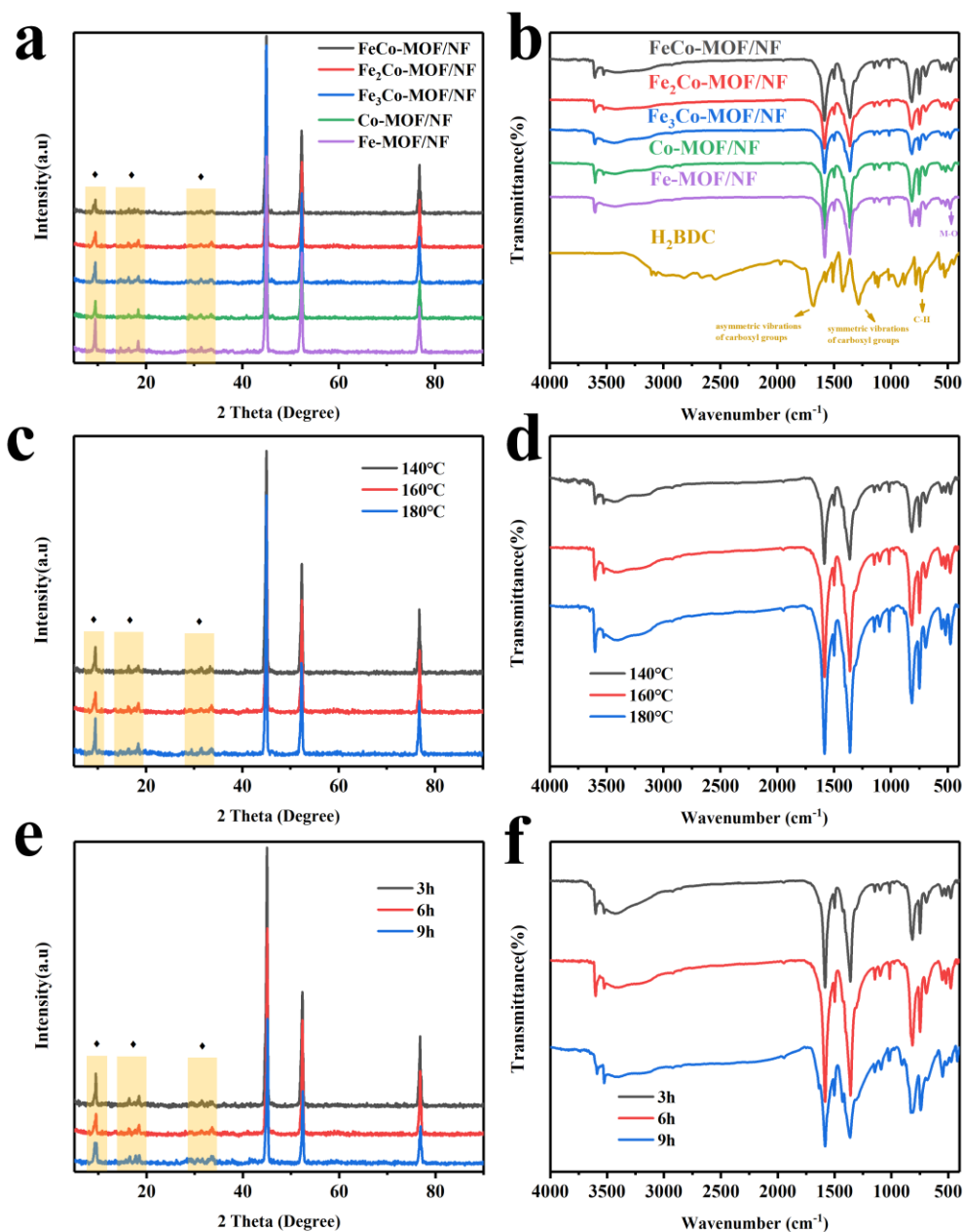

Fig. S8. SEM images of (a, b, c, d) Fe_2Co-MOF@M-OOHv-ER/NF-0.1 M KOH, and (e, f, g, h) Fe_2Co-MOF@M-OOHv-ER/NF-5 M KOH at 100um, 2um, 1um, and 500nm, respectively.

In addition, the SEM images of electrode materials with different cycles (2nd, 30th) and different KOH concentrations (0.1 M KOH, 5 M KOH) were also exhibited (Fig. S7 and S7). When the number of electro-oxidation cycles is 2nd, the small flakes are peeled off the surface of the material (Fig. S7a-d), and then when the number of active cycles is 30th, the morphology of the electrode becomes triangular stacked sheets with rough surface, but the regular appearance begins to be destroyed (Fig. S7e-h). When the electro-oxide constitution is carried out at a concentration of 0.1 M potassium hydroxide, the flakes on the nickel foam become more heavily accumulated triangles (Fig. S8a-d). On the contrary, when the concentration of electric activated potassium hydroxide is 5 M, the material falls off from the nickel foam (Fig. S8e-h). In summary, the Fe_2Co-MOF@M-OOHv-ER/NF with electro-oxidation cycles (20th) and the KOH concentrations (1 M KOH) has a regular triangular stacked morphology with a high specific surface area, which may have a high electrocatalytic activity.
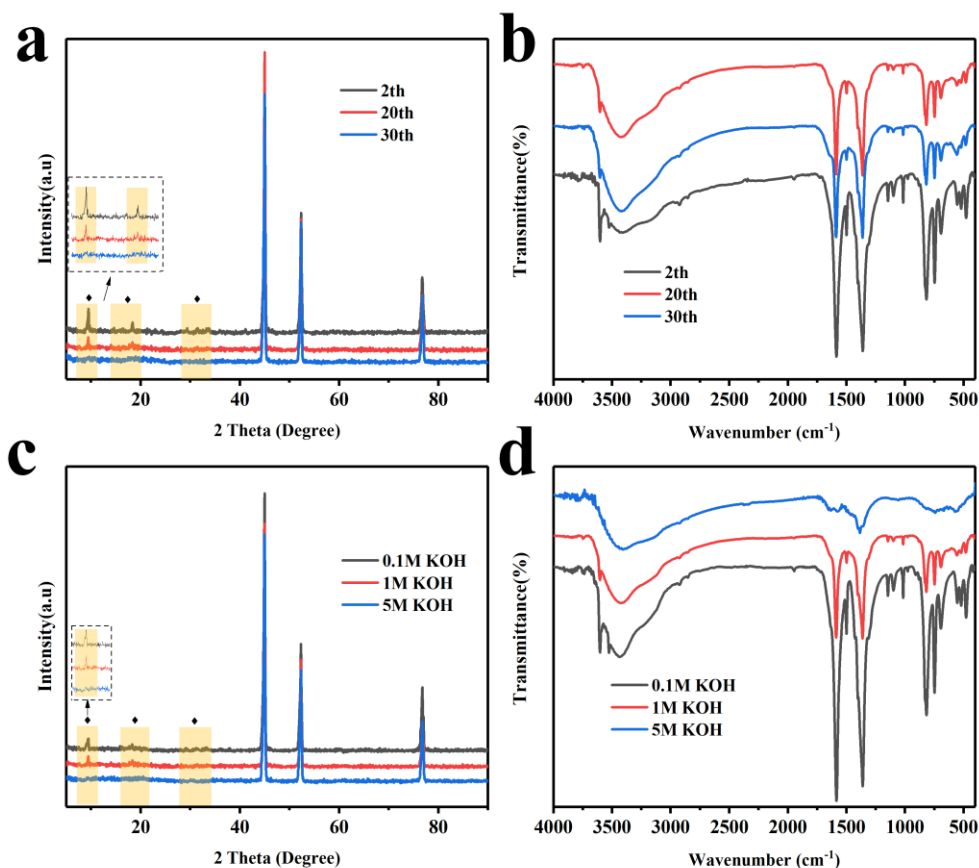
Fig. S9. SEM-EDX elemental mapping of (a, b, c, d, e, f) Fe$_2$Co-MOF/NF, and (g, h, i, j, k, l) Fe$_2$Co-MOF@M-OOHv-ER/NF.

Fig. S10. (a)XRD patterns of Fe/Co-MOF/NF samples with different mole ratios (Fe:Co = 1:0, 1:1, 2:1, 3:1, 0:1). (b) FT-IR spectrums of Fe/Co-MOF/NF samples with different mole ratios (Fe: Co = 1:0, 1:1, 2:1, 3:1, 0:1). (c)XRD patterns of Fe/Co-MOF/NF samples with different synthesis temperature (140 ℃, 160 ℃, 180 ℃). (d) FT-IR spectrums of Fe/Co-MOF/NF samples with different synthesis temperature (140 ℃, 160 ℃, 180 ℃). (e)XRD patterns of Fe/Co-MOF/NF samples with different synthesis time (3 h, 6 h, 9 h). (f) FT-IR spectrums of

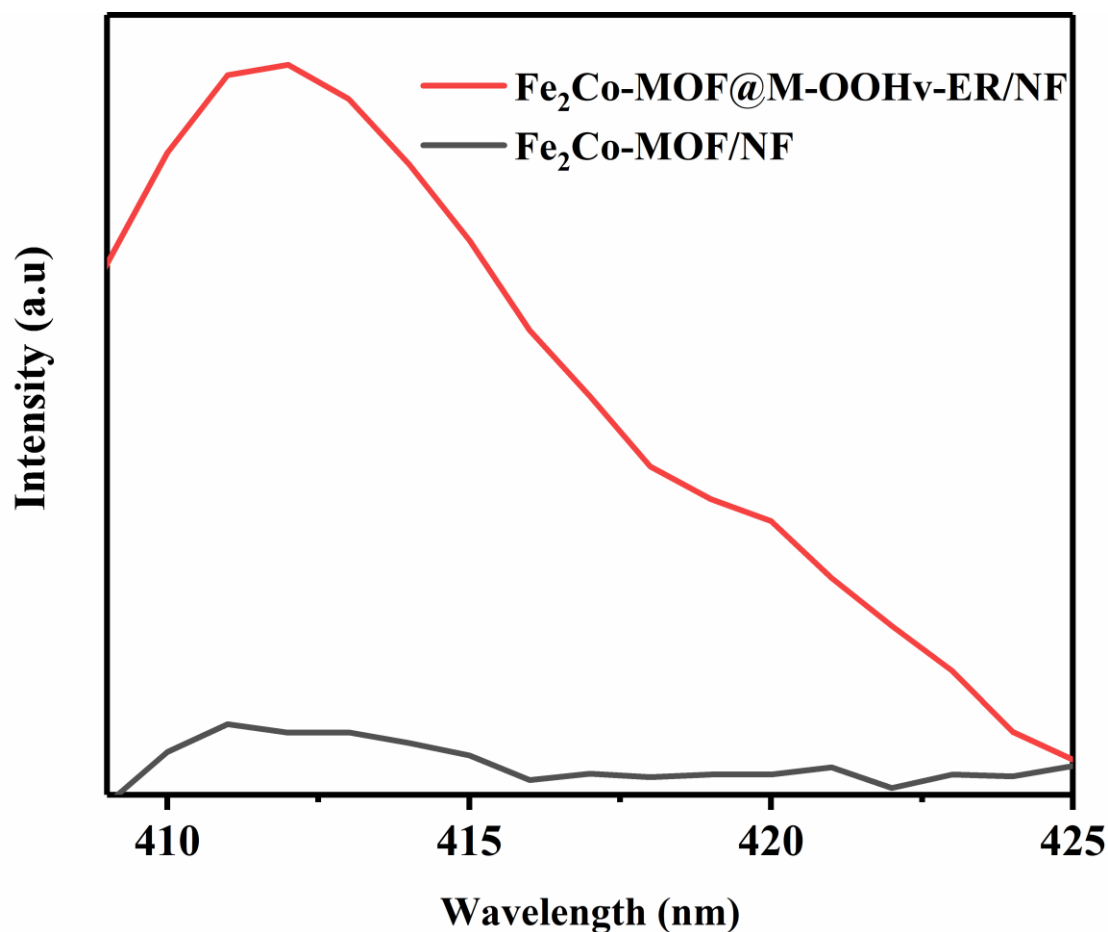Fe/Co-MOF/NF samples with different synthesis time (3 h, 6 h, 9 h).

Fig. S11. (a)XRD patterns of Fe$_2$Co-MOF@M-OOHv-ER/NF samples with different cycles (2nd, 20th, 30thth). (b) FT-IR spectrums of Fe$_2$Co-MOF@M-OOHv-ER/NF samples with different cycles (2nd, 20th, 30thth). (c)XRD patterns of Fe$_2$Co-MOF@M-OOHv-ER/NF samples with different KOH concentrations (0.1 M KOH, 1 M KOH, 5 M KOH). (d) FT-IR spectrums of Fe$_2$Co-MOF@M-OOHv-ER/NF samples with different KOH concentrations (0.1 M KOH, 1 M KOH, 5 M KOH).

XRD patterns of Fe/Co-MOF/NF samples with different mole ratios (Fe: Co = 1:0, 1:1, 3:1, 0:1), with different synthesis temperature (140 ℃, 180 ℃), and with different synthesis time (3

h, 9 h) are shown in Fig. S10 (a, c and e). The characteristic diffraction peaks of NF were located at 44.369°, 51.594° and 76.082°, corresponding to the (1 1 1), (2 0 0) and (2 2 0) planes of Ni, respectively (PDF No. 01-1258). Moreover, the three characteristic diffraction peaks shown in all the Fe/Co-MOF/NF samples were similar with minor offset, illustrating that they were formed on NF. As illustrated in the Fig. 1, the more obvious characteristic diffraction peaks a 9.5°, 16.3°, 18.4°, 32.8° and 33.4° were observed in all the Fe/Co-MOF/NF samples. Apart from the NF, the characteristic diffraction peaks of all the Fe/Co-MOF/NF samples are basically the same as those the Fe/Co-MOF (in literature), which prove the successful synthesis of all Fe/Co-MOF/NF samples. In addition, the molecular structure of all the Fe/Co-MOF/NF samples were also explored by Fourier transform infrared spectroscopy (FT-IR) in Fig. S10(b, d and f). The peaks at 1573 cm^{-1} and 1384 cm^{-1} of H_2BDC are corresponding to the asymmetric and symmetric vibrations of carboxyl groups, respectively. Moreover, the peaks at 746 cm^{-1} of H_2BDC assigned to C-H bonding vibrations of the benzene ring. In addition to the three characteristic peaks, the peaks at 476 cm^{-1} of all the Fe/Co-MOF/NF samples proved the formation of a metal-O bond between the carboxylic group of terephthalic acid and Fe or Co ions. The FT-IR results further illustrate the successful preparation of all Fe/Co-MOF/NF samples.
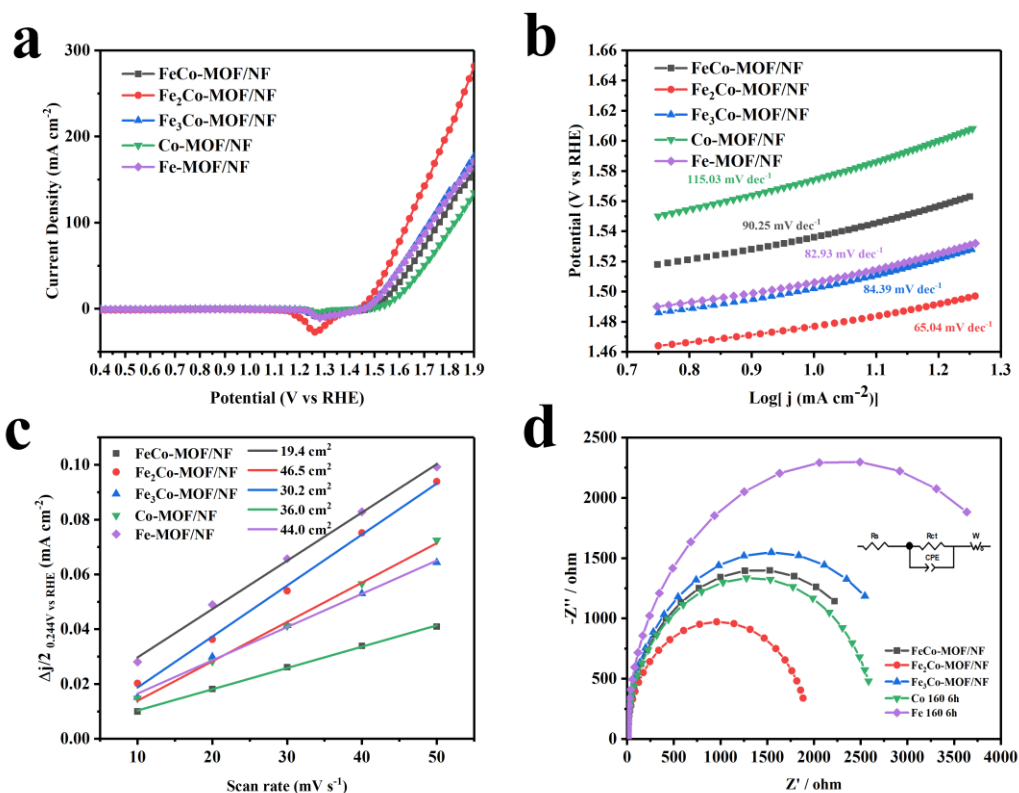
XRD patterns of all Fe_2Co-MOF@M-OOHv-ER/NF samples with different cycles (2nd, 20th, 30th), and with different synthesis temperature (140 °C, 160 °C, 180 °C) are shown in Fig. S11 (a and c). The characteristic diffraction peaks of Fe_2Co-MOF/NF become weaker with the increase of the number of cycles or concentration of potassium hydroxide, which proves that Fe_2Co-MOF may be converted into the M-OOHv, which could improve the oxygen evolution

performance. In addition, the molecular structure of all the Fe$_2$Co-MOF@M-OOHv-ER/NF samples were also explored by Fourier transform infrared spectroscopy (FT-IR) in Fig. S11 (b and d). The peaks at 1573 cm^{-1} and 1384 cm^{-1} of H$_2$BDC are corresponding to the asymmetric and symmetric vibrations of carboxyl groups, respectively. Moreover, the peaks at 746 cm^{-1} of H$_2$BDC assigned to C-H bonding vibrations of the benzene ring. The above characteristic peaks decrease with the increase of the number of cycles or the concentration of potassium hydroxide, which proves that Fe$_2$Co-MOF may be converted into the M-OOHv, which could improve the oxygen evolution performance. In addition, the peaks at 3400 cm^{-1} of all Fe$_2$Co-MOF@M-OOHv-ER/NF samples proved the formation of a metal-OH bond, which further proves that Fe$_2$Co-MOF was transformed to the M-OOHv.
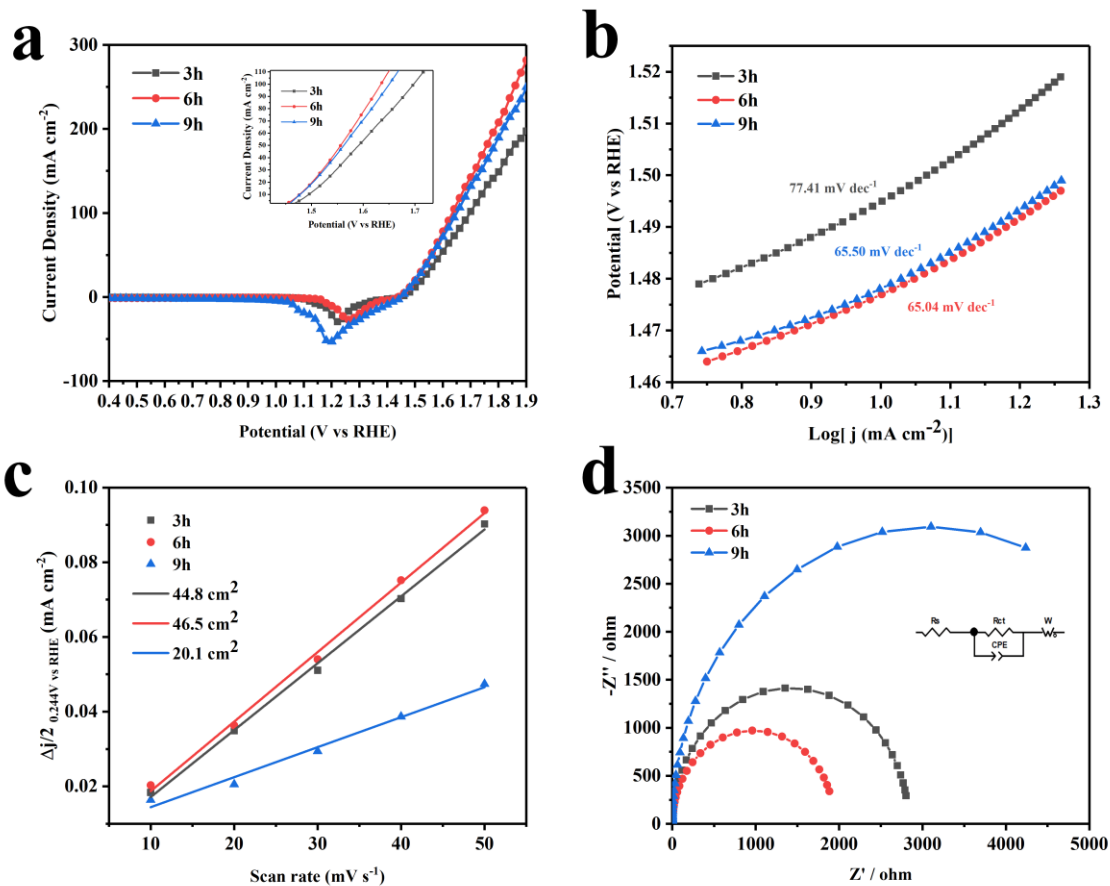

Fig. S12. Fluorescence spectra of Fe$_2$Co-MOF/NF, and Fe$_2$Co-MOF@M-OOHv-ER/NF at

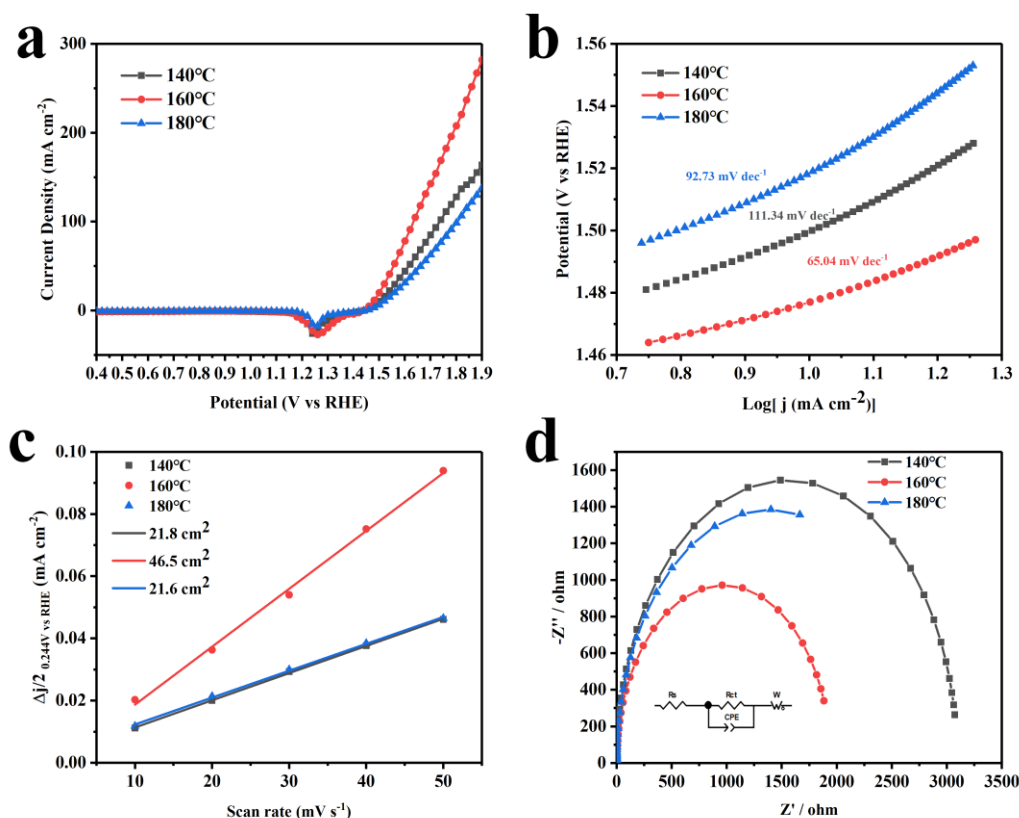excitation wavelengths of 285 nm.

Fig. S13. (a) IR-compensation LSV curves of Fe/Co-MOF/NF samples with different mole ratios (Fe:Co = 1:0, 1:1, 2:1, 3:1, 0:1) for OER in 1 M KOH. (b) Tafel slopes of the above electrodes. (c) Nyquist plots recorded at open circuit voltage in the frequency range from 100 kHz–0.01 Hz. (d) Plots used for evaluating the ECSA as a function of scan rate.

Fig. S14. (a) IR-compensation LSV curves of Fe/Co-MOF/NF samples with different synthesis time (3 h, 6 h, 9 h) for OER in 1 M KOH. (b) Tafel slopes of the above electrodes. (c) Nyquist plots recorded at open circuit voltage in the frequency range from 100 kHz–0.01 Hz. (d) Plots used for evaluating the ECSA as a function of scan rate.
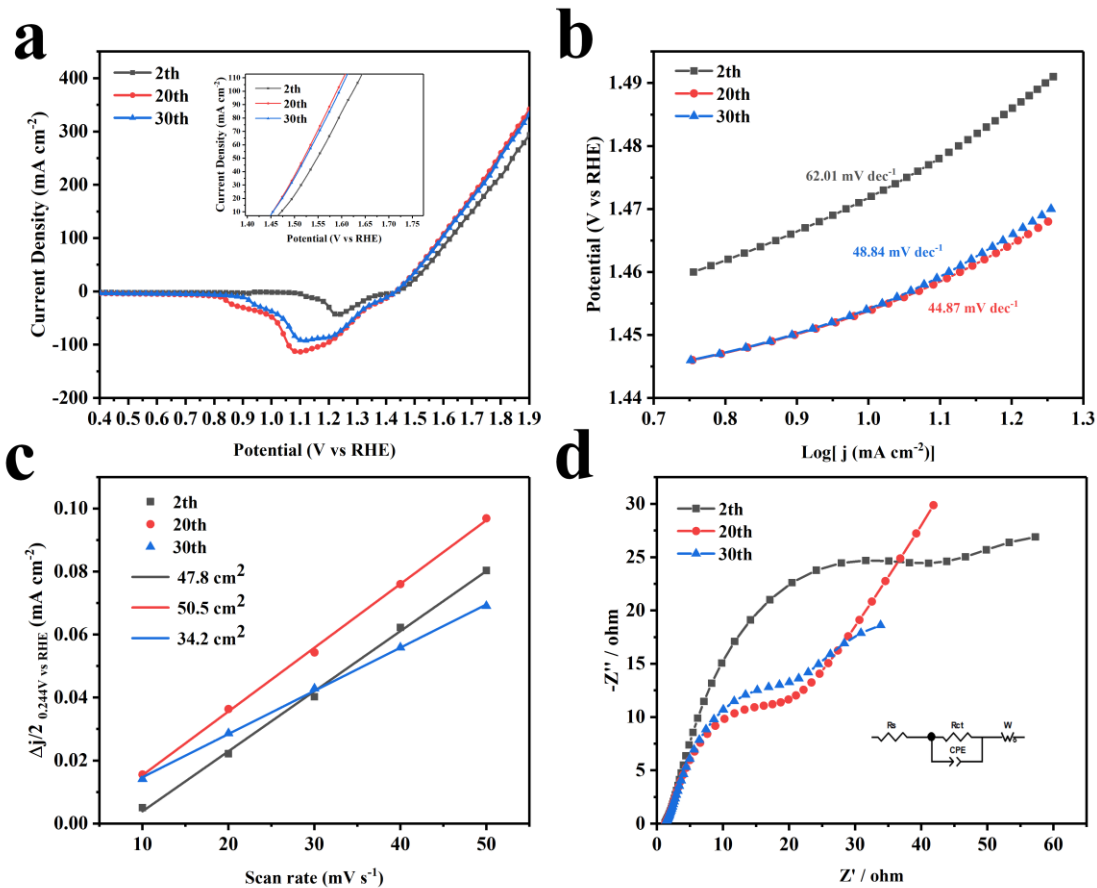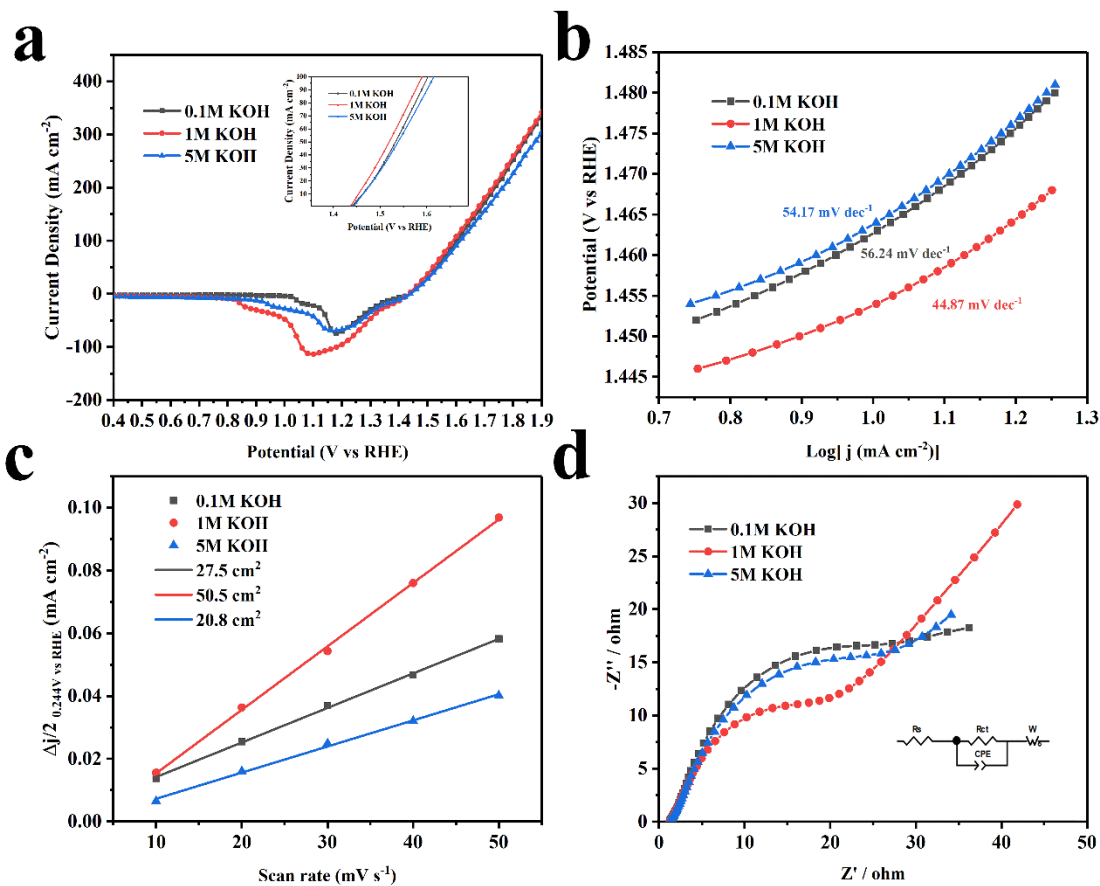
Fig. S15. (a) IR-compensation LSV curves of Fe/Co-MOF/NF samples with different synthesis temperature (140 °C, 160 °C, 180 °C) for OER in 1 M KOH. (b) Tafel slopes of the above electrodes. (c) Nyquist plots recorded at open circuit voltage in the frequency range from 100 kHz–0.01 Hz. (d) Plots used for evaluating the ECSA as a function of scan rate.

The OER performance was determined in 1 M KOH. Fig. S13, Fig. S14 and Fig. S15 show the OER electrocatalytic activity of Fe/Co-MOF/NF samples with different mole ratios (Fe: Co = 1:0, 1:1, 2:1, 3:1, 0:1), with different synthesis time (3 h, 6 h, 9 h), and different synthesis temperature (140 °C, 160 °C, 180 °C), respectively. As shown in the Table.S1, the Fe_2Co-MOF/NF electrode exhibits outstanding electrocatalytic efficiencies toward the OER with an η_{10} of only 247 mV and an η_{100} of only 405 mV, outperforming the Co-MOF/NF (η_{10} = 344 mV, η_{100} = 592 mV), Fe-MOF/NF (η_{10} = 276 mV, η_{100} = 499 mV), FeCo-MOF/NF (η_{10} = 306

mV, η_{100} = 530 mV), Fe$_3$Co-MOF/NF (η_{10} = 272 mV, η_{100} = 492 mV), Fe$_2$Co-MOF/NF-3 h (η_{10} = 265 mV, η_{100} = 468 mV), Fe$_2$Co-MOF/NF-9 h (η_{10} = 248 mV, η_{100} = 420 mV), Fe$_2$Co-MOF/NF-140 °C (η_{10} = 270 mV, η_{100} = 506 mV), and Fe$_2$Co-MOF/NF-180 °C (η_{10} = 288 mV, η_{100} = 575 mV). Furthermore, Fe$_2$Co-MOF/NF has the lower tafel value (65.04 mV dec^{-1}), the higher ECSA (46.5 cm^2), and the lower lowest charge transfer resistance (R$_{ct}$) (1944 Ω) than Co-MOF/NF (115.03 mV dec^{-1}, 36.0 cm^2, 2673 Ω), Fe-MOF/NF (82.93 mV dec^{-1}, 44.0 cm^2, 4609 Ω), FeCo-MOF/NF (90.25 mV dec^{-1}, 19.4 cm^2, 2809 Ω), Fe$_3$Co-MOF/NF (84.39 mV dec^{-1}, 30.2 cm^2, 3096 Ω), Fe$_2$Co-MOF/NF-3 h (77.41 mV dec^{-1}, 44.8 cm^2, 2832 Ω), Fe$_2$Co-MOF/NF-9 h (65.50 mV dec^{-1}, 20.1 cm^2, 6188 Ω), Fe$_2$Co-MOF/NF-140 °C (111.34 mV dec^{-1}, 21.8 cm^2, 3093 Ω), and Fe$_2$Co-MOF/NF-180 °C (92.73 mV dec^{-1}, 21.6 cm^2, 2770 Ω). And the best OER activity of Fe/Co-MOF/NF was achieved by the material with a mole ratio (Fe: Co = 2:1), a synthesis time of 6 h and a synthesis temperature of 160 °C. This was likely due to the fact that, for one thing, there were more active sites on the Fe$_2$Co-MOF/NF with a synthesis time of 6 h than that with a synthesis time of 3 h; and for another, overlap of the active sites may occur for the material with a synthesis time of 9 h, which reduced the OER activity. Likewise, on the one hand, there were more active sites on the Fe$_2$Co-MOF/NF with a synthesis temperature of 160 °C than that with a synthesis temperature of 140 °C; and on the other, overlap of the active sites may occur for the Fe$_2$Co-MOF/NF with a synthesis temperature of 180 °C, which decreased the OER activity. Thus, the following experiments were carried out using the Fe$_2$Co-MOF/NF with a synthesis time of 6 h and a synthesis temperature of 160 °C.
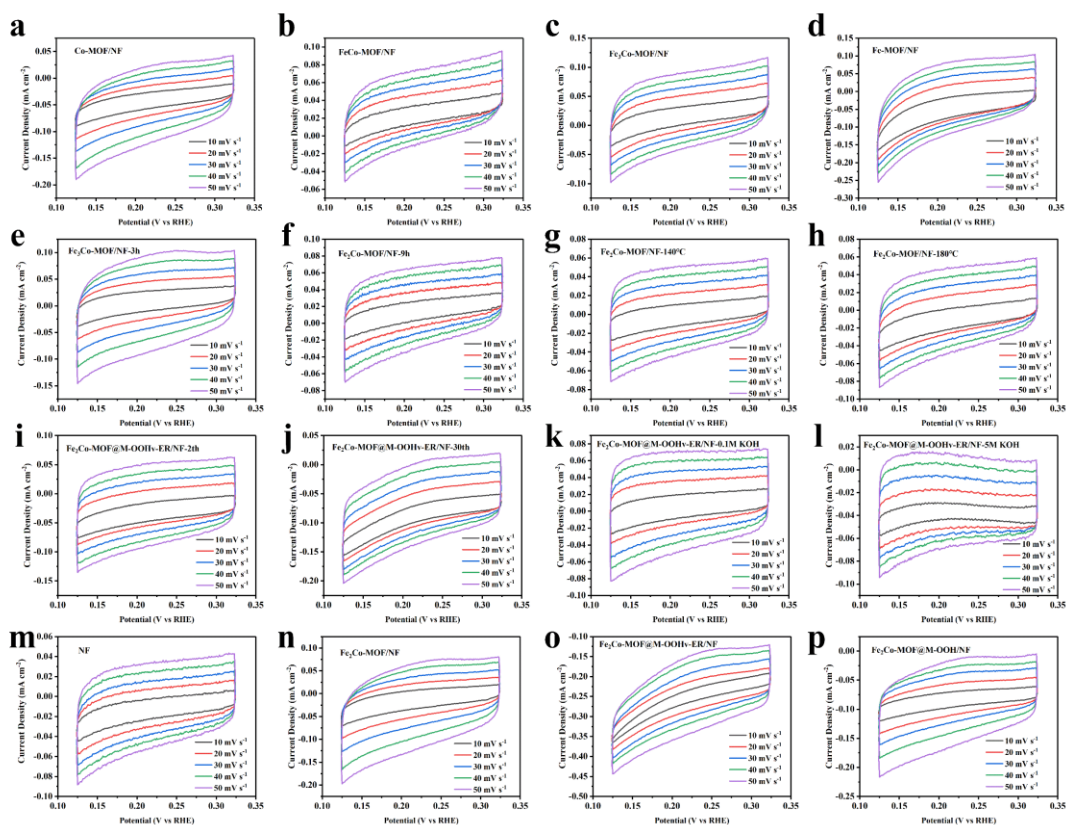
Fig. S16. (a) IR-compensation LSV curves of Fe$_2$Co-MOF@M-OOHv-ER/NF samples with different cycles (2nd, 20th, 30thth) for OER in 1 M KOH. (b) Tafel slopes of the above electrodes. (c) Nyquist plots recorded at open circuit voltage in the frequency range from 100 kHz–0.01 Hz. (d) Plots used for evaluating the ECSA as a function of scan rate.

Fig. S17. (a) IR-compensation LSV curves of Fe_2Co-MOF@M-OOHv-ER/NF samples with different KOH concentrations (0.1 M KOH, 1 M KOH, 5 M KOH) for OER in 1 M KOH. (b) Tafel slopes of the above electrodes. (c) Nyquist plots recorded at open circuit voltage in the frequency range from 100 kHz–0.01 Hz. (d) Plots used for evaluating the ECSA as a function of scan rate.
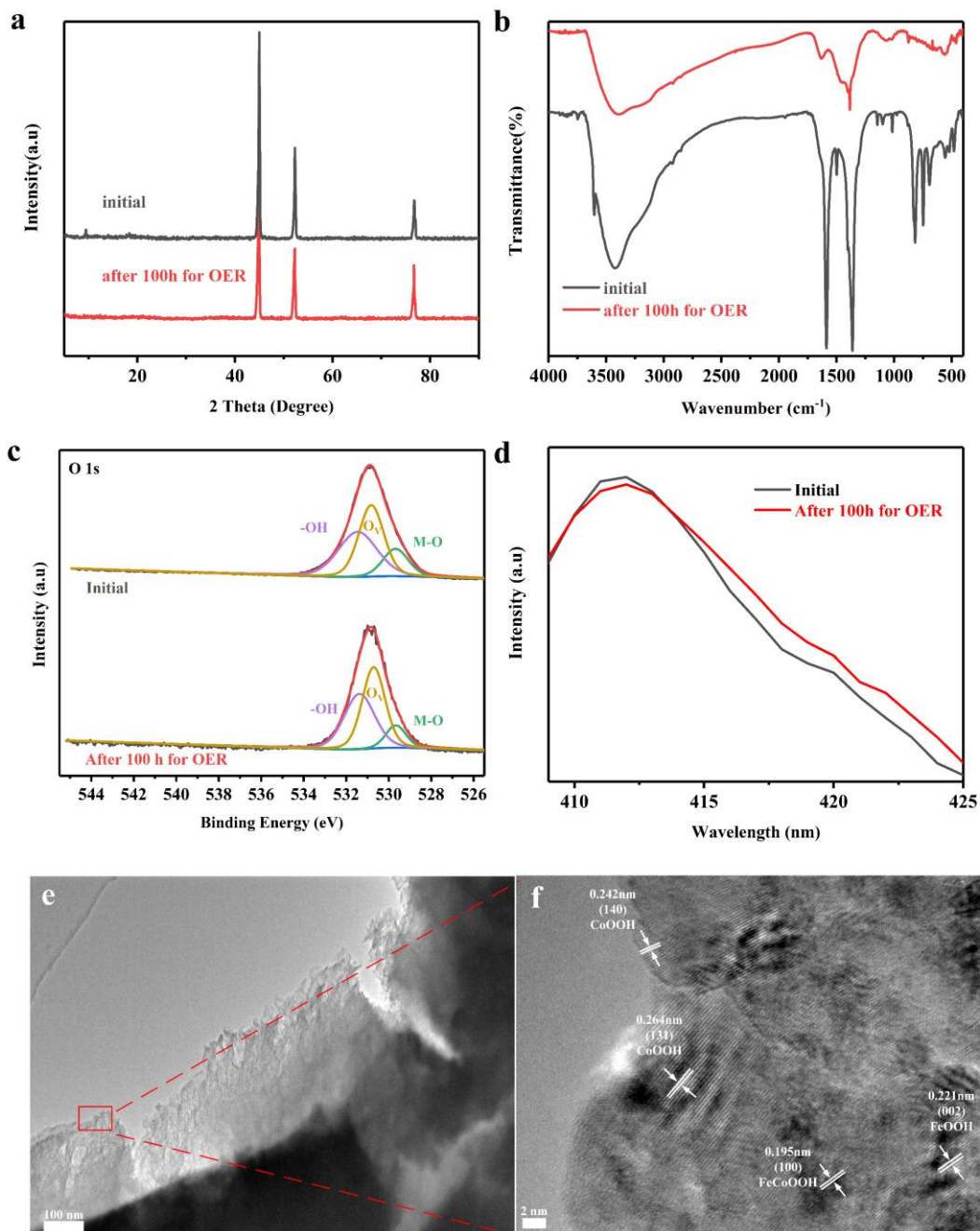
Fig. S16 and Fig. S17 show the OER electrocatalytic activity of Fe_2Co-MOF@M-OOHv-ER/NF obtained with different cycles (2nd, 20th, 30th) and different KOH concentrations (0.1 M KOH, 1 M KOH, 5 M KOH), respectively. As shown in the Table.S1, the Fe_2Co-MOF@M-OOHv-ER/NF electrode exhibits outstanding electrocatalytic efficiencies toward the OER with an η_{10} of only 224 mV and an η_{100} of only 360 mV, outperforming the Fe_2Co-MOF@M-OOHv-

ER/NF-2nd (η_{10} = 242 mV, η_{100} = 394 mV), Fe$_2$Co-MOF@M-OOHv-ER/NF-30th (η_{10} = 224 mV, η_{100} = 365 mV), Fe$_2$Co-MOF@M-OOHv-ER/NF-0.1 M KOH (η_{10} = 233 mV, η_{100} = 372 mV), and Fe$_2$Co-MOF@M-OOHv-ER/NF-5 M KOH (η_{10} = 234 mV, η_{100} = 385 mV). Furthermore, Fe$_2$Co-MOF@M-OOHv-ER/NF has the lower tafel value (44.87 mV dec^{-1}), the higher ECSA (50.5 cm^2) and the lower R$_{ct}$ (11.11Ω) than Fe$_2$Co-MOF@M-OOHv-ER/NF-2nd (62.01 mV dec^{-1}, 7.2 cm^2, 31.60 Ω), Fe$_2$Co-MOF@M-OOHv-ER/NF-30th (44.84 mV dec^{-1}, 34.2 cm^2, 13.18 Ω), Fe$_2$Co-MOF@M-OOHv-ER/NF-0.1 M KOH (56.24 mV dec^{-1}, 27.5 cm^2, 19.81 Ω), Fe$_2$Co-MOF@M-OOHv-ER/NF-0.1 M KOH (54.17 mV dec^{-1}, 20.8 cm^2, 15.93 Ω). This was likely due to the fact that, for one thing, there were more active sites on the Fe$_2$Co-MOF@M-OOHv-ER/NF with cycles of 20th than that with cycles of 2nd; and for another, overlap of the active sites may occur for the Fe$_2$Co-MOF@M-OOHv-ER/NF with cycles of 20th, which reduced the OER activity. Likewise, on the one hand, there were more active sites on the Fe$_2$Co-MOF@M-OOHv-ER/NF with a KOH concentration of 1 M than that a KOH concentration of 0.1 M; and on the other, overlap of the active sites may occur for the material with a KOH concentration of 5 M, which decreased the OER activity. Thus, the following electro-oxide reconstitution experiments were carried out using the Fe$_2$Co-MOF/NF as the precursor with a cycle of 20th and a KOH concentration of 1 M.
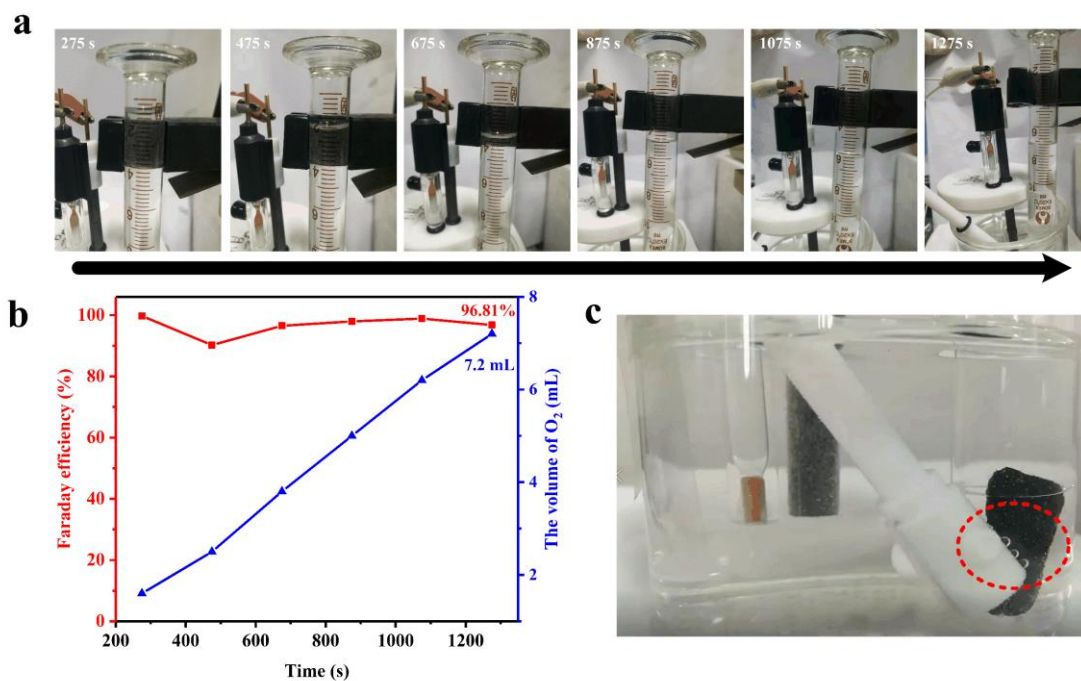
Fig. S18. (a) CV curves of Co-MOF/NF; (b) CV curves of FeCo-MOF/NF;(c) CV curves of Fe$_3$Co-MOF/NF; (d) CV curves of Fe-MOF/NF; (e) CV curves of Fe$_2$Co-MOF/NF-3 h; (f) CV curves of Fe$_2$Co-MOF/NF-9 h; (g) CV curves of Fe$_2$Co-MOF/NF-140 °C;(h) CV curves of Fe$_2$Co-MOF/NF-180 °C; (i) CV curves of Fe$_2$Co-MOF@M-OOHv-ER/NF-2nd; (j) CV curves of Fe$_2$Co-MOF@M-OOHv-ER /NF-30thth; (k) CV curves of Fe$_2$Co-MOF@M-OOHv-ER/NF-0.1 M KOH; (l) CV curves of Fe$_2$Co-MOF@M-OOHv-ER/NF-5 M KOH; (m) CV curves of NF; (n) CV curves of Fe$_2$Co-MOF/NF; (o) CV curves of Fe$_2$Co-MOF@M-OOHv-ER/NF; (P) CV curves of Fe$_2$Co-MOF@M-OOHv/NF at increasing scan rates from 10 mV s^{-1} to 50 mV s^{-1}.
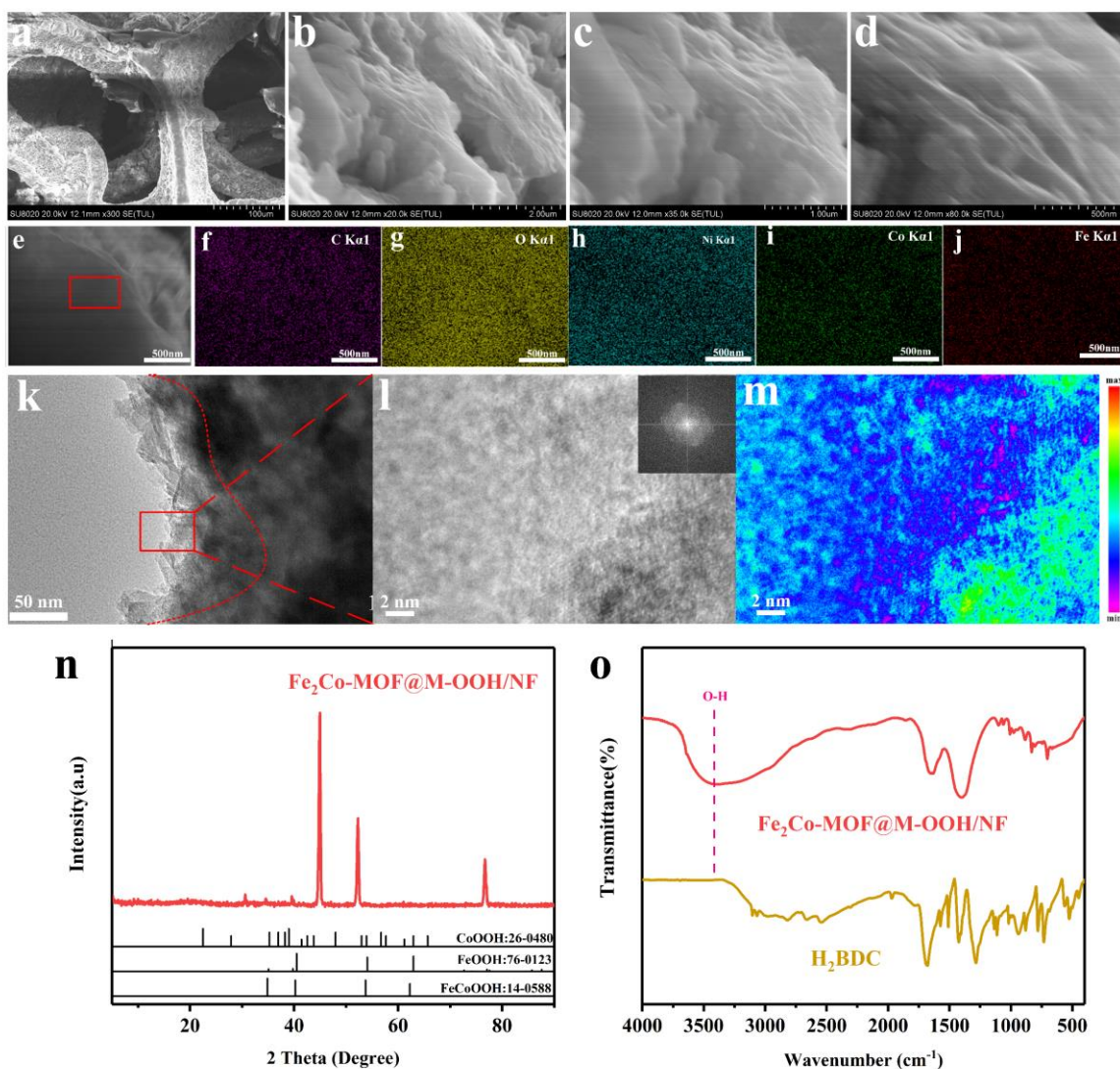
Fig. S19. (a) XRD patterns of Fe$_2$Co-MOF@M-OOHv-ER/NF before and after the stability test;

(b) FTIR patterns of Fe$_2$Co-MOF@M-OOHv-ER/NF before and after the stability test; (c) XPS

patterns for the O 1s of Fe$_2$Co-MOF@M-OOHv-ER/NF before and after the stability test; (d)

PL patterns of Fe$_2$Co-MOF@M-OOHv-ER/NF before and after the stability test. TEM images

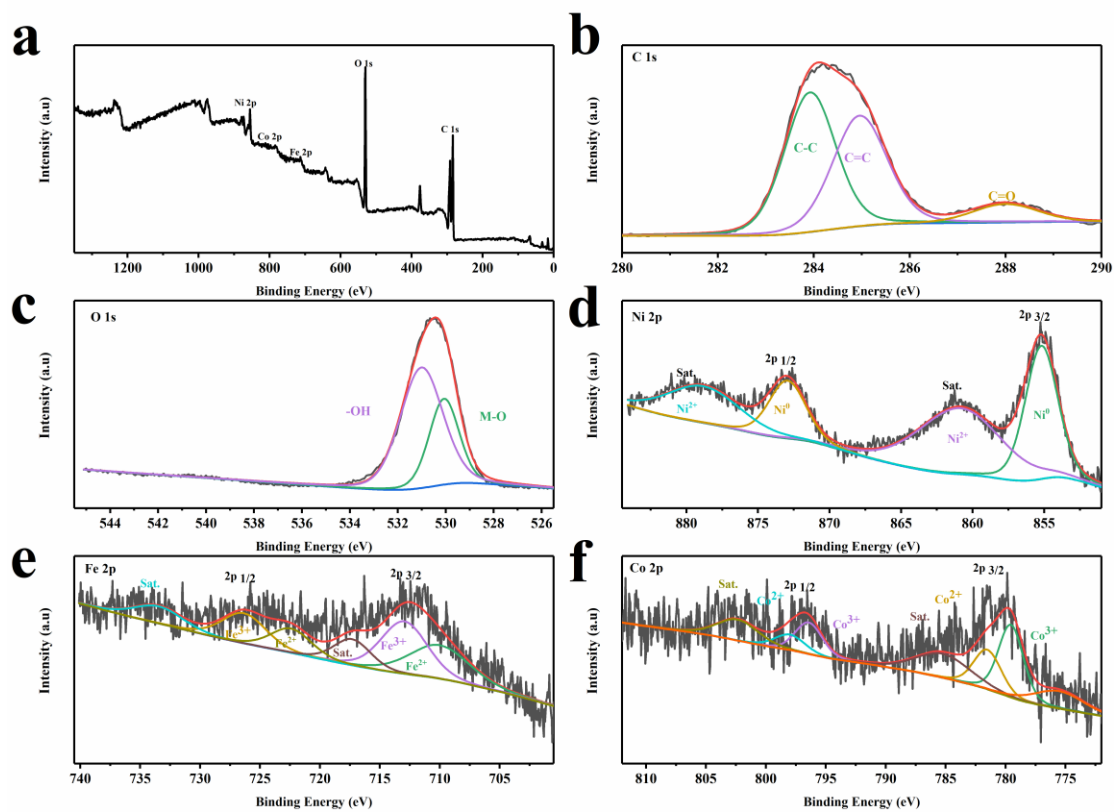of (e, f) Fe$_2$Co-MOF@M-OOHv-ER/NF after the stability test.

Fig. S20. (a) Photographs of oxygen collected at various reaction times. (b) Faraday efficiency and the volume of O_2 of the Fe$_2$Co-MOF@M-OOHv-ER/NF for OER at various reaction time. (c) The photograph of Faraday efficiency test.
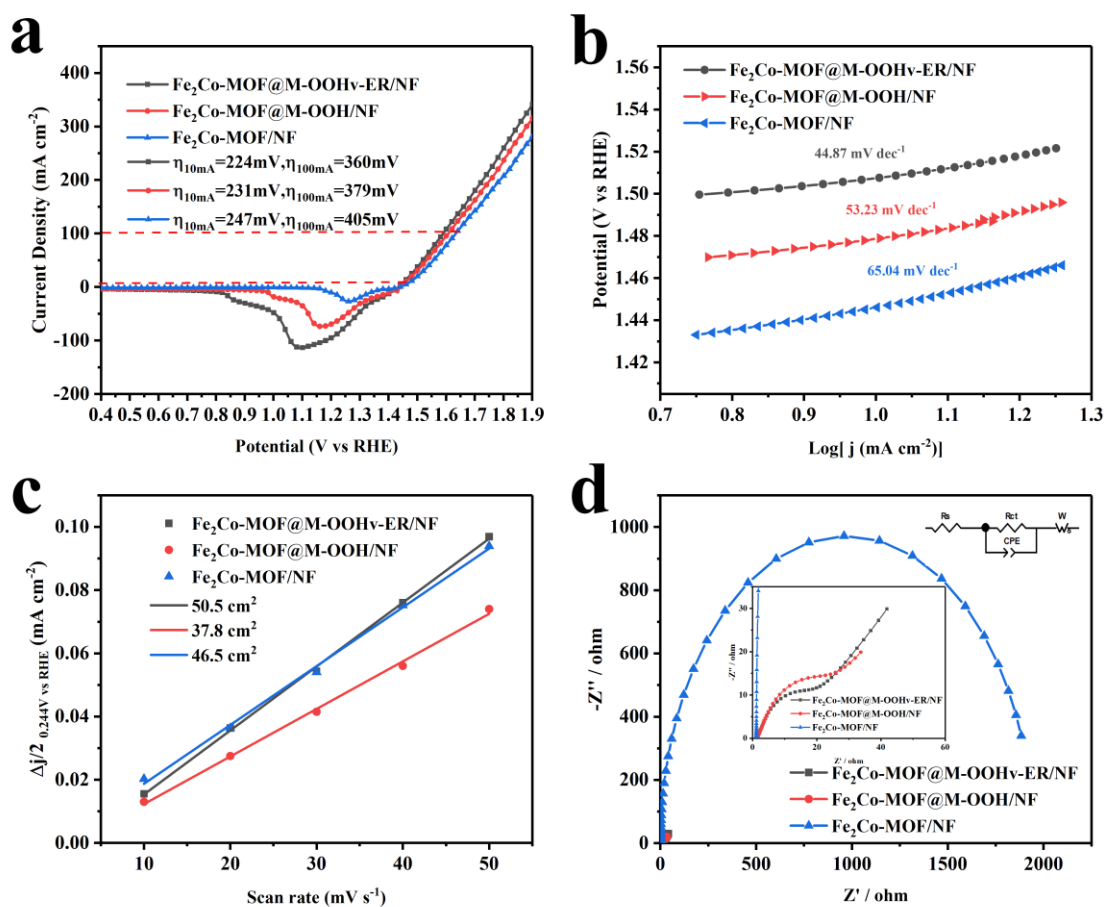
Fig. S21. SEM images of (a, b, c, d) Fe$_2$Co-MOF@M-OOHv-ER/NF at 100um, 2um, 1um, and 500nm, respectively. SEM-EDX elemental mapping of (e, f, g, h, i, j) Fe$_2$Co-MOF@M-OOHv-ER/NF. TEM and HR-TEM images of (k, l) Fe$_2$Co-MOF@M-OOHv-ER/NF. (m) Strain map of Fe$_2$Co-MOF@M-OOHv-ER/NF. (n)XRD pattern of Fe$_2$Co-MOF@M-OOHv-ER/NF. (o) FT-IR spectrum of Fe$_2$Co-MOF@M-OOHv-ER/NF.

Fig. S22. (a) XPS full survey of Fe$_2$Co-MOF@M-OOH/NF. HR-XPS spectra of (b) C1s, (c) O1s, (d) Ni2p, (e) Fe2p, and (f) Co2p of Fe$_2$Co-MOF@M-OOH/NF.
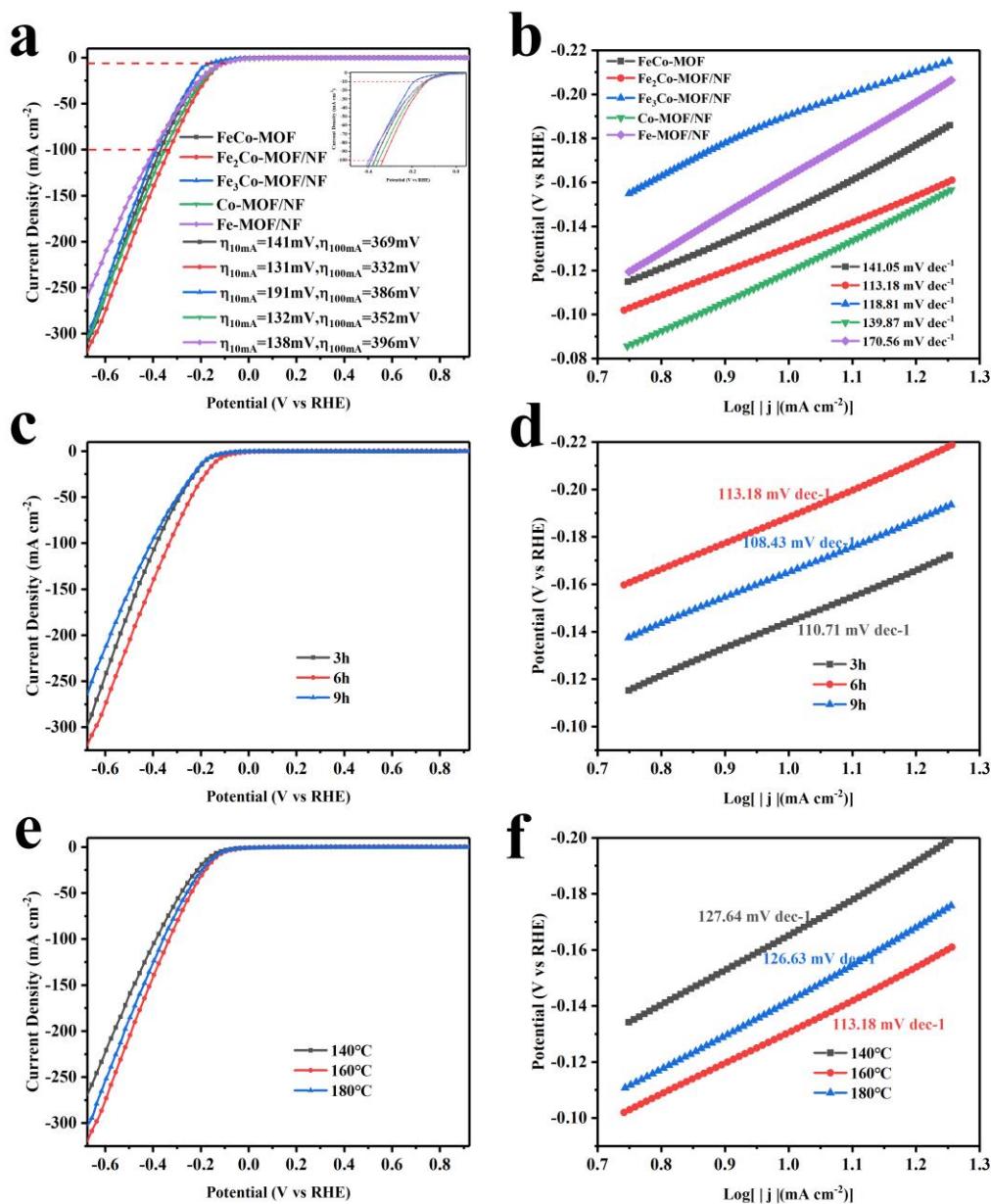
Fig. S23. (a) IR-compensation LSV curves of $Fe_2Co-MOF/NF$, $Fe_2Co-MOF@M-OOH/NF$ and $Fe_2Co-MOF@M-OOHv-ER/NF$ for OER in 1 M KOH. (b) Tafel slopes of the above electrodes. (c) Nyquist plots recorded at open circuit voltage in the frequency range from 100 kHz–0.01 Hz. (d) Plots used for evaluating the ECSA as a function of scan rate.

In order to further explore the excellent properties of the nanonet structure prepared by the electro-oxidation reconstitution, the $Fe_2Co-MOF@M-OOH$ without electro-oxidation was obtained by soaking in 1 M KOH solution for 6 hours. The surface and edges of $Fe_2Co-MOF@M-OOH/NF$ become rough and uneven along with the flaky morphology is destroyed (Fig. S21a-d), but the distribution of all metal elements is uniform (Fig. S21e-j), and new amorphous substances without defects are formed on the surface (Fig. S21k-m). Through

further analysis of the XRD and FTIR, the amorphous substance on the surface of Fe_2Co-MOF@M-OOH/NF may be metal-oxyhydroxide (M-OOH) (Fig. S21n and S19o). In the alkaline solution, metal ions will separate out, and the M-OOH may be generated in situ on the surface of Fe_2Co-MOF/NF. Through the XPS analysis of Fe_2Co-MOF@M-OOH/NF, the elements contained in Fe_2Co-MOF@M-OOH/NF have not changed (Fig. S22a). However, the O1s of Fe_2Co-MOF@M-OOH/NF only contains two peaks, the M-O and the -OH from M-OOH; and there is no oxygen-defect peak, indicating that the Fe_2Co-MOF@M-OOH/NF does not contain oxygen defects (Fig. S22c).
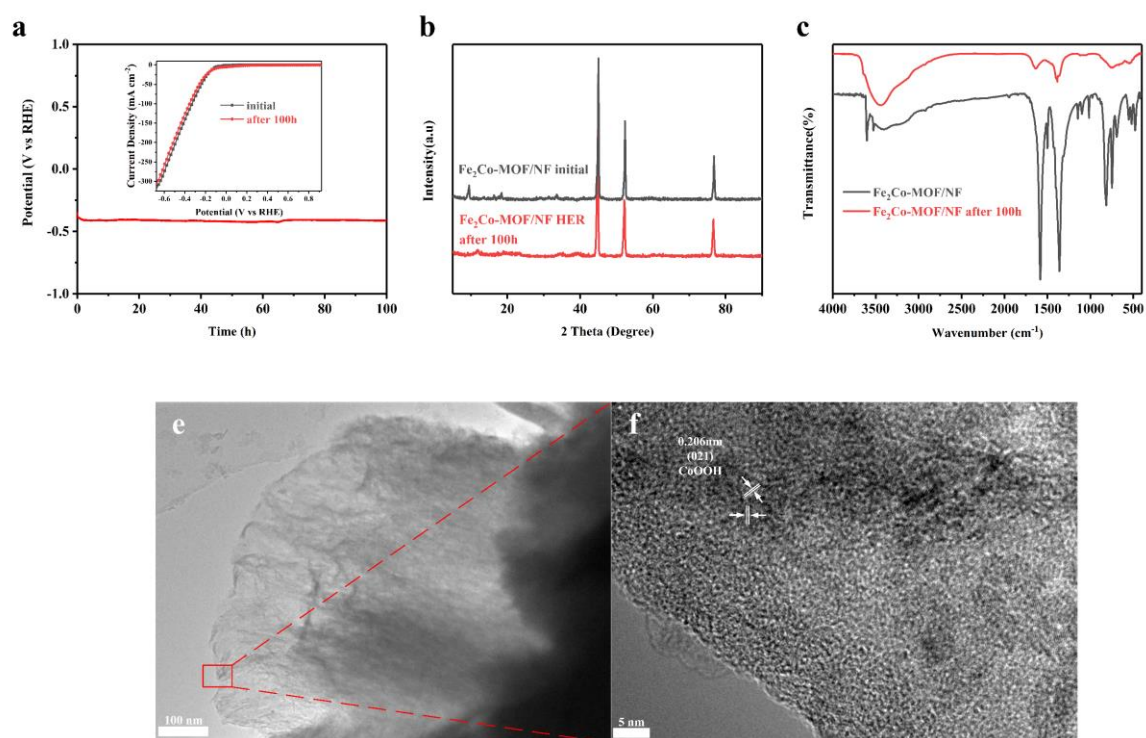
In order to explore the changes of oxygen evolution performance, the LSV of Fe_2Co-MOF@M-OOH/NF was also tested. Notably, the oxygen evolution overpotential of Fe_2Co-MOF@M-OOH/NF (η_{10} = 231 mV, η_{100} = 379 mV) is higher than the Fe_2Co-MOF@M-OOHv-ER/NF (η_{10} = 224 mV, η_{100} = 360 mV), but lower than the Fe_2Co-MOF/NF (η_{10} = 247 mV, η_{100} = 405 mV). In order to further study the reasons for the changes in the oxygen evolution performance of Fe_2Co-MOF@M-OOH/NF, the Tafel, ECSA and EIS of Fe_2Co-MOF@M-OOH were also tested. Similarly, the tafel value, ECSA and Rct of Fe_2Co-MOF@M-OOH /NF (55.23 mV dec^{-1}, 37.8 cm^2, 14.38 Ω) are all lower than the Fe_2Co-MOF/NF (65.04 mV dec^{-1}, 46.5 cm^2, 1944 Ω), but higher than the Fe_2Co-MOF@M-OOHv-ER/NF (44.87 mV dec^{-1}, 50.5 cm^2, 11.11 Ω). One hand, the amorphous M-OOH formed on the surface of Fe_2Co-MOF@M-OOH/NF is the real oxygen evolution site, which improves the reaction kinetics of Fe_2Co-MOF@M-OOH/NF and reduces the resistance, thereby improving the oxygen evolution performance; on the other hand, the amorphous M-OOH formed on the surface of Fe_2Co-MOF@M-OOH/NF does not contain oxygen defects and the flaky morphology is corroded by the alkaline solution, which limits the

further improvement of its oxygen evolution performance.

Fig. S24. (a) IR-compensation LSV curves of Fe/Co-MOF/NF samples with different mole ratios (Fe:Co = 1:0, 1:1, 2:1, 3:1, 0:1) for OER in 1 M KOH. (b) Tafel slopes of the above electrodes. (c) IR-compensation LSV curves of Fe/Co-MOF/NF samples with different synthesis time (3 h, 6 h, 9 h) for OER in 1 M KOH. (d) Tafel slopes of the above electrodes. (e) IR-compensation LSV curves of Fe/Co-MOF/NF samples with different synthesis temperature

(140 °C, 160 °C, 180 °C) for OER in 1 M KOH. (f) Tafel slopes of the above electrodes.


Fig. S25. (a) Stability test for HER at 100 mA cm^{-2} by Fe$_2$Co-MOF/NF electrode in 1 M KOH solution. (b) XRD patterns of Fe$_2$Co-MOF/NF before and after the stability test; (c) FTIR patterns of Fe$_2$Co-MOF/NF before and after the stability test. TEM images of (e, f) Fe$_2$Co-MOF/NF after the stability test.

The HER performance was determined in 1 M KOH. Fig. S24 shows the HER electrocatalytic activity of Fe/Co-MOF/NF samples with different mole ratios (Fe: Co = 1:0, 1:1, 2:1, 3:1, 0:1), with different synthesis time (3 h, 6 h, 9 h), and different synthesis temperature (140 °C, 160 °C, 180 °C), respectively. As shown in the Table.S2, the Fe$_2$Co-MOF/NF electrode exhibits outstanding electrocatalytic efficiencies toward the HER with an η_{10} of only 131 mV and an η_{100} of only 332 mV, outperforming the Co-MOF/NF (η_{10} = 132 mV, η_{100} = 352 mV), Fe-

MOF/NF (η_{10} = 138 mV, η_{100} = 396 mV), FeCo-MOF/NF (η_{10} = 141 mV, η_{100} = 369 mV), Fe$_3$Co-MOF/NF (η_{10} = 191 mV, η_{100} = 386 mV), Fe$_2$Co-MOF/NF-3 h (η_{10} = 178 mV, η_{100} = 385 mV), Fe$_2$Co-MOF/NF-9 h (η_{10} = 183 mV, η_{100} = 409 mV), Fe$_2$Co-MOF/NF-140 °C (η_{10} = 158 mV, η_{100} = 388 mV), and Fe$_2$Co-MOF/NF-180 °C (η_{10} = 139 mV, η_{100} = 358 mV). Furthermore, Fe$_2$Co-MOF/NF has the lower tafel value (113.18 mV dec^{-1}) than Co-MOF/NF (139.87 mV dec^{-1}), Fe-MOF/NF (170.56 mV dec^{-1}), FeCo-MOF/NF (141.05 mV dec^{-1}), Fe$_3$Co-MOF/NF (118.81 mV dec^{-1}), Fe$_2$Co-MOF/NF-3 h (110.71 mV dec^{-1}), Fe$_2$Co-MOF/NF-9 h (108.43 mV dec^{-1}), Fe$_2$Co-MOF/NF-140 °C (127.64 mV dec^{-1}), and Fe$_2$Co-MOF/NF-180 °C (126.63 mV dec^{-1}). Thus, the following experiments were carried out using the Fe$_2$Co-MOF/NF with a synthesis time of 6 h and a synthesis temperature of 160 °C. Besides the excellent activities, the long-term stability is also critically important for a potential electrocatalyst for practical applications. When estimated by galvanostatic measurement at an industrial constant current of 100 mA cm^{-2}, Fe$_2$Co-MOF/NF could remain nearly no decay within 100 h (Fig. S25a). In addition, the excellent durability of Fe$_2$Co-MOF/NF is further verified by the LSV curves, in which the performance after the stability test is slightly reduced (inset of Fig. S25a). Moreover, the XRD and FTIR of the Fe$_2$Co-MOF/NF electrode after 100 h for HER have changed compared with that before the stability test (Fig. S25a and b), which is attributed to the formation of alkaline oxyhydroxides on the surface through the TEM image after the stability test. On one hand, this explains why the hydrogen evolution performance dropped slightly after the stability test. On the other hand, due to the protective effect of the cathodic current, the amount of alkaline oxyhydroxide generated on the surface of Fe$_2$Co-MOF/NF after

the stability test is small (Fig. S25c and d), which slightly affects its hydrogen evolution

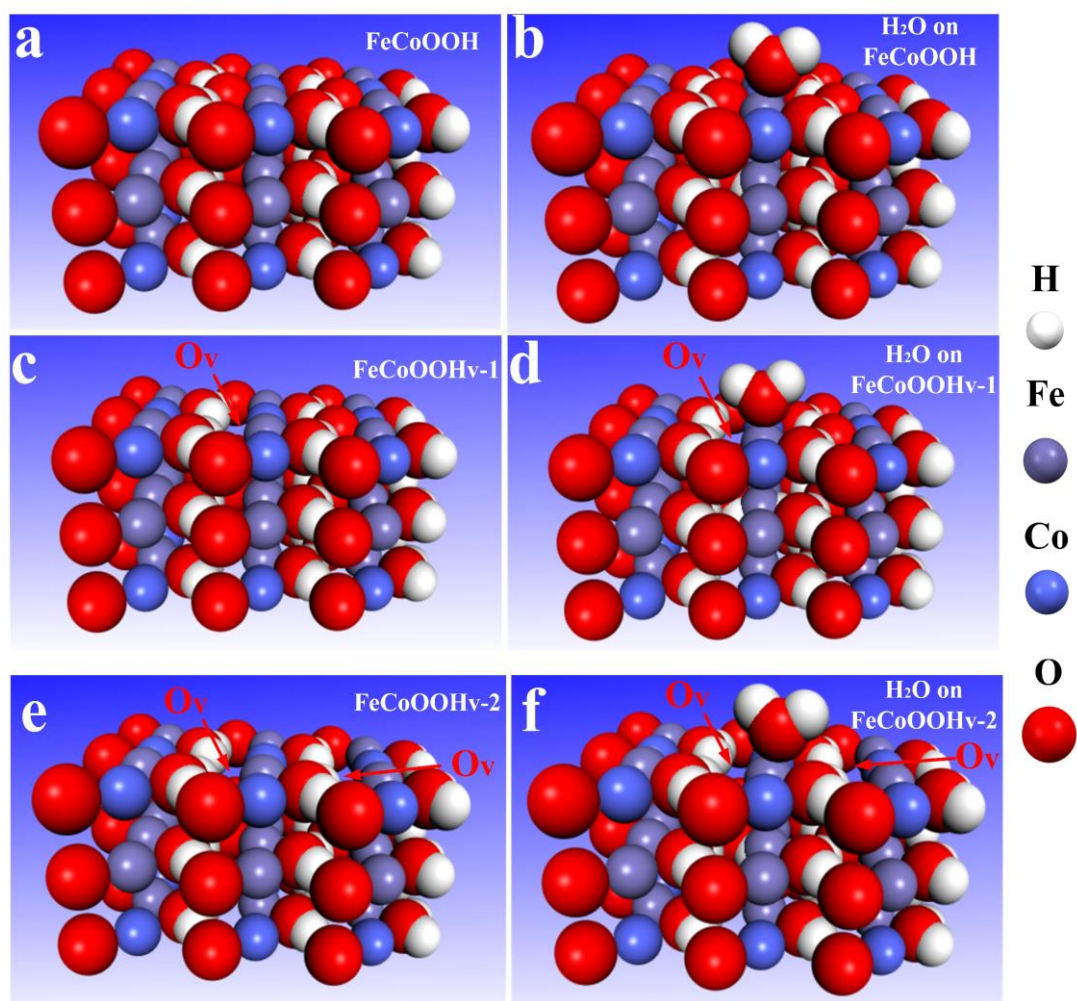performance, so it still has a relatively high stability overall.
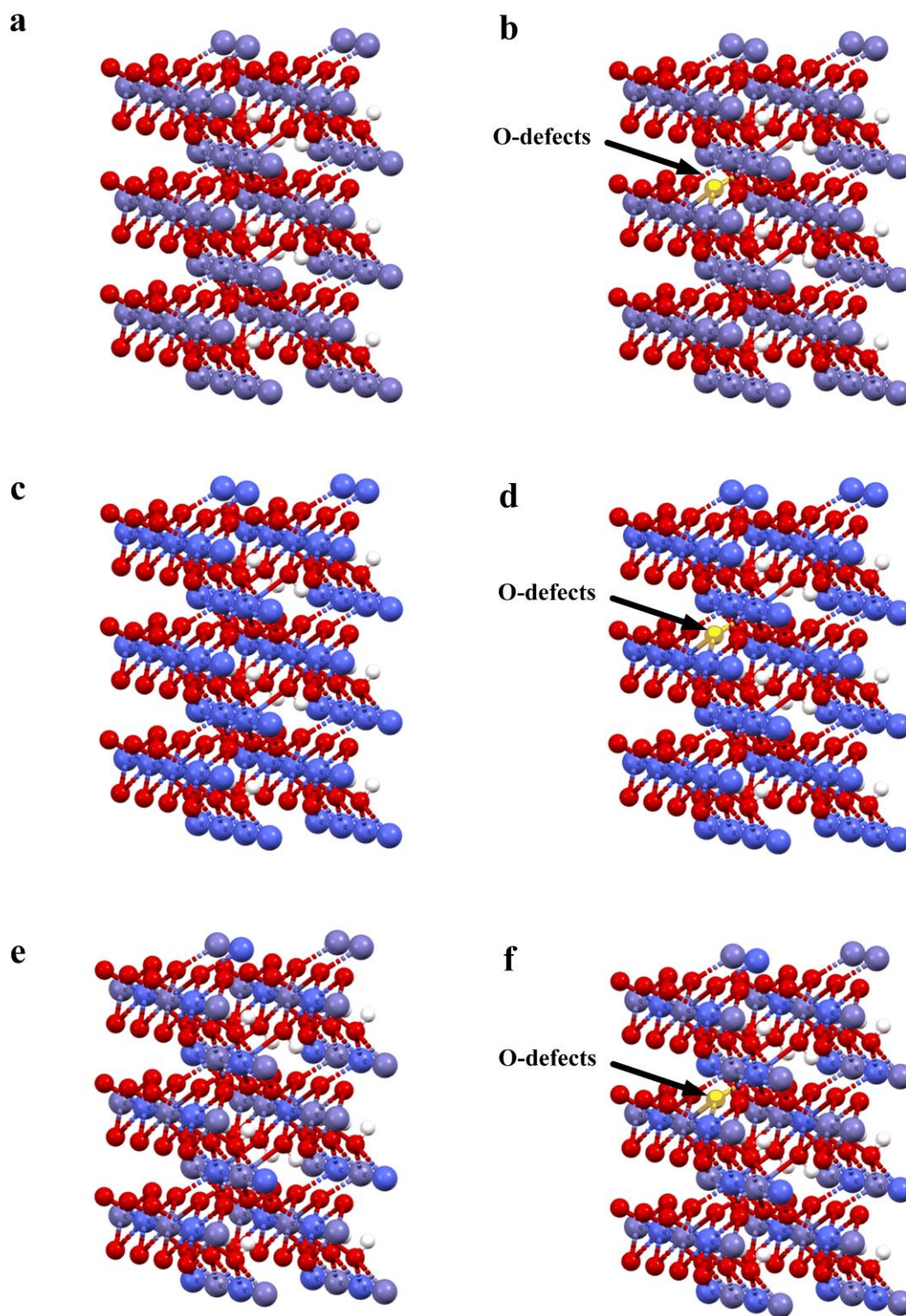
Fig. S26. Schematic drawings of the crystal structures of (a) FeOOH, (b) FeOOHv, (c) CoOOH, (d) CoOOHv, (e) FeCoOOH, and (f) FeCoOOHv. The Fe, Co, O and H atoms are represented by gray, cyan, red and white spheres, respectively.
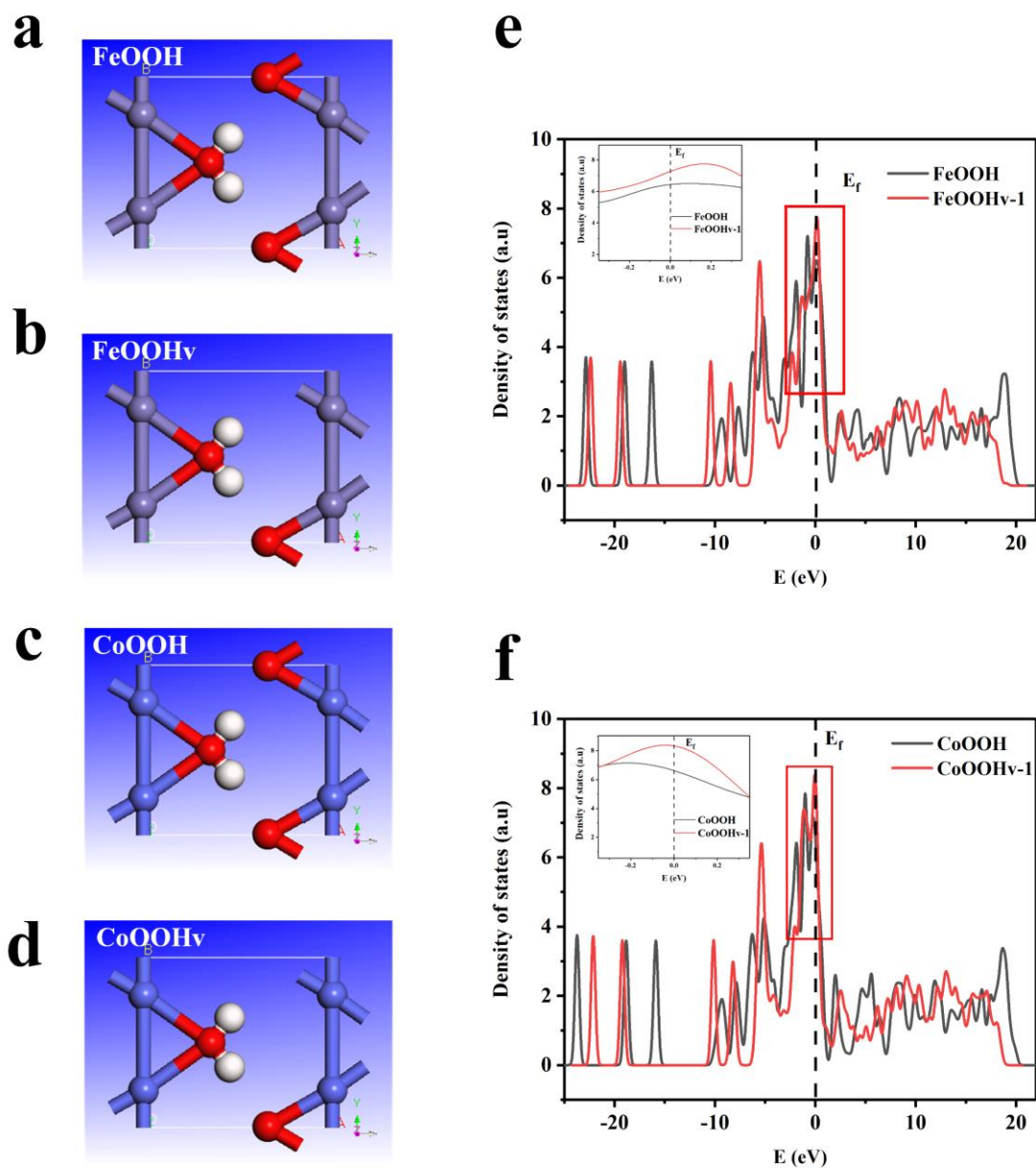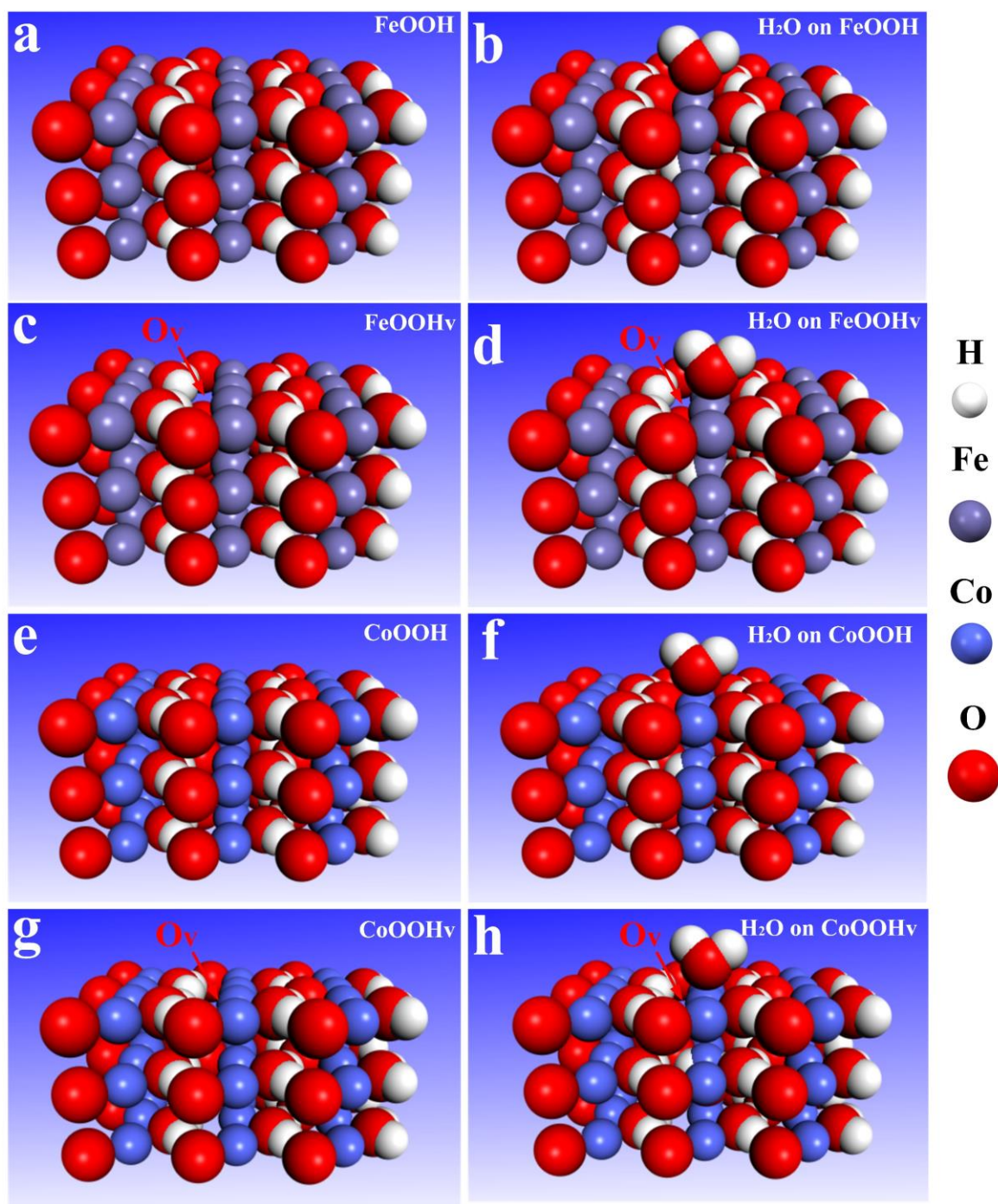
Fig. S27. Schematic drawings of the crystal structures of unit cell of (a) FeOOH, (b) FeOOHv, (c) CoOOH and (d) CoOOHv. (e) The projected density of states and band structure of FeOOH and FeOOHv structures. (f) The projected density of states and band structure of CoOOH and CoOOHv structures. The Fe, Co, O and H atoms are represented by gray, cyan, red and white spheres, respectively.

To further shed light on the mechanism of how surficial oxygen defects influence electron density of states around the Fermi level (E_f) in M-OOH, the first-principle calculations based on well-resolved density functional theory (DFT) were performed.The models of FeOOH and FeOOH with oxygen defects (FeOOHv) after the structural optimization are shown in the Fig. S27 (a and b), respectively. Moreover, the structural optimization model of CoOOH and CoOOH with oxygen defects (CoOOHv) are shown in the Fig. S27 (c and d), separately. The density of states diagrams of FeOOH, FeOOHv, CoOOH and CoOOHv could be calculated from these models. The electronic density of state of FeOOHv at the Fermi level is higher than that of FeOOH (Fig. S27e). Similarly, the electronic density of state of CoOOHv at the Fermi level is higher than that of CoOOH (Fig. S27f). In summary, these indicate that oxygen defects could regulate the distribution of electronic state density and increase the local electronic state density, thereby accelerating electron transfer and improving catalytic performance.

Fig. S28. The adsorption energy of water molecules on the surface of FeCoOOH (a, b), FeCoOOHv-1 (c, d), and FeCoOOHv-2 (e, f). The Fe, Co, O and H atoms are represented by gray, cyan, red and white spheres, respectively.

Fig. S29. The adsorption energy of water molecules on the surface of FeOOH (a, b), FeOOHv (c, d), CoOOH (e, f) and CoOOHv (g, h). The Fe, Co, O and H atoms are represented by gray, cyan, red and white spheres, respectively.

Fig. S30. Photographs of the contact angle of Fe$_2$Co-MOF@M-OOHv-ER/NF with the H$_2$O.

Table. S1 The ratios of Fe^{3+}/Fe^{2+} and Co^{3+}/Co^{2+} of the Fe_2Co-MOF/NF and Fe_2Co-MOF@M-OOHv-ER/NF integrated from the XPS, respectively.

Catalysts	Area (Fe^{3+})	Area (Fe^{2+})	Ratio (Fe^{3+}/Fe^{2+})	Area (Co^{3+})	Area (Co^{2+})	Ratio (Co^{3+}/Co^{2+})
Fe_2Co-MOF/NF	17973.5695	12557.09025	1.431348	5801.612	8465.58625	0.685317
Fe_2Co-MOF@M-OOHv-ER/NF	24912.8435	5185.058	4.804738	18373.9875	14518.7165	1.265538

Table. S2 The OER overpotentials and Tafel values of the electrodes.

Catalysts	η_{10} (mV)	η_{100} (mV)	Tafel (mV dec^{-1})
Co-MOF/NF	344	592	115.03
Fe-MOF/NF	276	499	82.93
FeCo-MOF/NF	306	530	90.25
Fe$_3$Co-MOF/NF	272	492	84.39
Fe$_2$Co-MOF/NF-3 h	265	468	77.41
Fe$_2$Co-MOF/NF-9 h	248	420	65.50
Fe$_2$Co-MOF/NF-140 ℃	270	506	111.34
Fe$_2$Co-MOF/NF-180 ℃	288	575	92.73
Fe$_2$Co-MOF@M-OOHv-ER/NF-2nd	242	394	62.01
Fe$_2$Co-MOF@M-OOHv-ER/NF-30th	224	365	48.84
Fe$_2$Co-MOF@M-OOHv-ER/NF-0.1 M KOH	233	372	56.24
Fe$_2$Co-MOF@M-OOHv-ER/NF-5 M KOH	234	385	54.17
NF	433	-	176.34
Fe$_2$Co-MOF/NF	247	405	65.04
Fe$_2$Co-MOF@M-OOH/NF	231	379	53.23
Fe$_2$Co-MOF@M-OOHv-ER/NF	224	360	44.87

Table. S3 The ECSAs values and EIS values of the electrodes.

Catalysts	ECSA (cm^2)	Rs (ohm)	Rct (ohm)
NF	19.7	1.23	7093
Fe$_2$Co-MOF/NF	46.5	1.19	1944
FeCo-MOF/NF	19.4	1.56	2809
Fe$_3$Co-MOF/NF	30.2	1.35	3096
Fe-MOF/NF	44.0	1.72	4609
Co-MOF/NF	36.0	1.16	2673
Fe$_2$Co-MOF/NF-3 h	44.8	1.45	2832
Fe$_2$Co-MOF/NF-9 h	20.1	1.42	6188
Fe$_2$Co-MOF/NF-140 ℃	21.8	1.84	3093
Fe$_2$Co-MOF/NF-180 ℃	21.6	1.48	2770
Fe$_2$Co-MOF@M-OOHv-ER/NF	50.5	1.22	11.11
Fe$_2$Co-MOF@M-OOH/NF	37.8	1.20	14.38
Fe$_2$Co-MOF@M-OOHv-ER/NF-2nd	47.8	1.20	31.60
Fe$_2$Co-MOF@M-OOHv-ER/NF-30th	34.2	1.20	13.18
Fe$_2$Co-MOF@M-OOHv-ER/NF-0.1 M KOH	27.5	1.21	19.81
Fe$_2$Co-MOF@M-OOHv-ER/NF-5 M KOH	20.8	1.20	15.93

Table.S4 The HER overpotentials and Tafel values of the electrodes.

Catalysts	η_{10} (mV)	η_{100} (mV)	Tafel (mV dec^{-1})
Co-MOF/NF	132	352	139.87
FeCo-MOF/NF	141	369	141.05
Fe$_2$Co-MOF/NF	131	332	113.18
Fe$_3$Co-MOF/NF	191	386	118.81
Fe-MOF/NF	138	396	170.56
Fe$_2$Co-MOF/NF-3 h	178	385	110.71
Fe$_2$Co-MOF/NF-9 h	183	409	108.43
Fe$_2$Co-MOF/NF-140 ℃	158	388	127.64
Fe$_2$Co-MOF/NF-180 ℃	139	358	126.63

Table. S5 The total energy and the adsorption energy of water molecules of FeCoOOH, FeCoOOHv-1, FeCoOOHv-2.

Simulation	Total Energy (Ev)
H_2O molecule	-471.882566
FeCoOOH	-3309.78959
FeCoOOHv-1	-2870.27626
FeCoOOHv-2	-2492.28674
H_2O on FeCoOOH	-3782.43125
H_2O on FeCoOOHv-1	-3343.17296
H_2O on FeCoOOHv-2	-2965.66533
ΔE_{ad}(FeCoOOH)	-0.759094
ΔE_{ad}(FeCoOOHv-1)	-1.014134
ΔE_{ad}(FeCoOOHv-2)	-1.496024

Table. S6 The total energy and the adsorption energy of water molecules of FeOOH, CoOOH, FeOOHv, CoOOHv.

Simulation	Total Energy (Ev)
H_2O molecule	-471.882566
FeOOH	-3068.77103
CoOOH	-3542.45755
FeOOHv	-2633.32322
CoOOHv	-3107.05715
H_2O on FeOOH	-3541.20253
H_2O on CoOOH	-4014.97586
H_2O on FeOOHv	-3106.00742
H_2O on CoOOHv	-3579.83865
$\Delta E_{ad}(FeOOH)$	-0.548934
$\Delta E_{ad}(CoOOH)$	-0.635744
$\Delta E_{ad}(FeOOHv)$	-0.801634
$\Delta E_{ad}(CoOOHv)$	-0.898934

Table. S7 Comparison of electrochemical performances of OER of Fe$_2$Co-MOF@M-OOHv-ER/NF with recently reported top tier metal based inorganic OER electrocatalysts in 1 M KOH.

Catalysts	η_{10} (mV)	Tafel slope (mV dec^{-1})	Ref.
Fe$_2$Co-MOF@M-OOHv-ER/NF	**224**	**44.3**	**This work**
CoOOH hollow nanospheres	275	49	J. Mater. Chem. A 2019, 7, 7777-7783.[1]
CoOOH NS	253	87	Energ. Environ. Sci. 2019, 12, 739-746.[2]
Co-FeOOH/CFP	250	36	Small 2019, 15, 1901015.[3]
NNU-23 (Fe2Ni)	365	81.8	Angew. Chem. Int. Ed. 2018, 57, 1-6.[4]
Ni$_3$FeN/r-GO-NF	270	54	ACS Nano 2018, 12, 245.[5]
Co$_5$ $_{Mo1.0}$O NSs@NF	270	54.4	Nano Energy 2018, 45, 448.[6]
VOOH/NF	270	68	Angew. Chem. 2017, 56, 573.[7]
Cu$_3$N/NF	286	118	ACS Energy Lett. 2019, 4, 747.[8]
FeB$_2$-NF	296	52.4	Adv. Energy Mater. 2017, 7, 1700513.[9]
FeSe$_2$/NF	245	-	Angew. Chem. 2017, 56, 10506.[10]

References

1. H. Wang, E.-m. Feng, Y.-m. Liu and C.-y. Zhang, *Journal of Materials Chemistry A*, 2019, **7**, 7777-7783.

2. J. Zhou, Y. Wang, X. Su, S. Gu, R. Liu, Y. Huang, S. Yan, J. Li and S. Zhang, *Energy & Environmental Science*, 2019, **12**, 739-746.

3. X. Han, C. Yu, J. Yang, X. Song, C. Zhao, S. Li, Y. Zhang, H. Huang, Z. Liu, H. Huang, X. Tan and J. Qiu, *Small*, 2019, **15**, 1901015.

4. X.-L. Wang, L.-Z. Dong, M. Qiao, Y.-J. Tang, J. Liu, Y. Li, S.-L. Li, J.-X. Su and Y.-Q. Lan, *Angewandte Chemie International Edition*, 2018, **57**, 9660-9664.

5. Y. Gu, S. Chen, J. Ren, Y. A. Jia, C. Chen, S. Komarneni, D. Yang and X. Yao, *ACS Nano*, 2018, **12**, 245-253.

6. Y. Zhang, Q. Shao, S. Long and X. Huang, *Nano Energy*, 2018, **45**, 448-455.

7. H. Shi, H. Liang, F. Ming and Z. Wang, *Angewandte Chemie International Edition*, 2017, **56**, 573-577.

8. C. Panda, P. W. Menezes, M. Zheng, S. Orthmann and M. Driess, *ACS Energy Letters*, 2019, **4**, 747-754.

9. H. Li, P. Wen, Q. Li, C. Dun, J. Xing, C. Lu, S. Adhikari, L. Jiang, D. L. Carroll and S. M. Geyer, *Advanced Energy Materials*, 2017, **7**, 1700513.

10. C. Panda, P. W. Menezes, C. Walter, S. Yao, M. E. Miehlich, V. Gutkin, K. Meyer and M. Driess, *Angewandte Chemie International Edition*, 2017, **56**, 10506-10510.